

Detecting the neutrino mass via the cross-correlation between matter tracers and the ISWRS effect?

Viviana Cuozzo,^{a,b} Marina Migliaccio,^{a,b} Matteo Calabrese,^c Carmelita Carbone^d

^aUniversità degli Studi di Roma Tor Vergata, via della Ricerca Scientifica 1, I-00133 Roma, Italy

^bINFN, Sezione di Roma 2, Università degli Studi di Roma Tor Vergata, via della Ricerca Scientifica 1, I-00133 Roma, Italy

^cAstronomical Observatory of the Autonomous Region of the Aosta Valley (OAVdA), Loc. Lignan 39, I-11020, Nus (Aosta Valley), Italy

^dINAF – Istituto di Astrofisica Spaziale e Fisica cosmica di Milano (IASF-MI), via Alfonso Corti 12, I-20133 Milano, Italy

E-mail: vcuozzo@roma2.infn.it

Abstract. This work explores the potential to detect the nonlinear Integrated Sachs Wolfe effect, namely the Rees-Sciama effect (ISWRS), by cross-correlating current and future Cosmic Microwave Background (CMB) experiments—Simons Observatory, CMB-S4, CMB-HD, and PICO—with ongoing Large Scale Structure (LSS) surveys, such as Euclid and the Vera Rubin Observatory (LSST). We model the cross-correlation of the ISWRS effect with gravitational potential tracers like galaxy clustering, cosmic shear, and CMB-lensing potential, to forecast results from these experiments. Our analysis also accounts for the presence of massive neutrinos to assess the feasibility of identifying the $\nu\Lambda$ CDM model and constraining the neutrino mass sum, M_ν . Our findings indicate that the CMB-lensing potential reconstructed by CMB-HD is expected to provide the most promising results, achieving $\gtrsim 5\sigma$ detections even under conservative assumptions for detector noise and foregrounds, thereby allowing differentiation between $\nu\Lambda$ CDM models. Galaxy clustering can also yield significant detections, whereas cosmic shear can provide valuable results only if non-linearities are accurately modelled, beyond the capabilities of currently available analytical approaches. These latter LSS probes do not provide strong constraining power on M_ν . While our findings suggest that future CMB experiments and LSS surveys will enable the detection of the ISWRS effect, they do not imply significant prospects for imposing new constraints on neutrino masses in the near future.

Contents

1	Introduction	1
2	Theoretical Framework	2
2.1	Integrated Sachs Wolfe and Rees Sciama Effects	2
2.2	Cross-correlation with matter tracers in the presence of massive neutrinos	3
3	Detectability of the ISWRS effect and identification of $\nu\Lambda$DM model	6
3.1	Ideal forecasts	8
3.2	Realistic forecasts for future CMB Experiments and LSS Surveys	10
3.3	Galaxy clustering – Optimal Weighting	12
3.3.1	Euclid photometric (GC) \times ISWRS	14
3.3.2	LSST “Gold” (GC) \times ISWRS	14
3.3.3	LSST “Optimistic” (GC) \times ISWRS	15
3.4	Cosmic Shear	16
3.4.1	Euclid photometric (CS) \times ISWRS	16
3.4.2	N-body simulation analysis	16
3.5	CMB-Lensing	17
3.5.1	CMBL \times ISWRS	17
4	Conclusions and discussion	18
A	Validation of the ISWRS cross-correlation with CS	21
B	Cross angular power spectra	21

1 Introduction

Modern cosmology deals with several open questions. First among the others, the nature of Dark Energy (DE; e.g., [1]). Some of the unresolved issues are intertwined with the Standard Model of particle physics, such as the value of the sum of the three neutrino masses, $M_\nu = \sum m_\nu$, whose tightest bounds come in fact from cosmological data [2–6]. The Integrated Sachs-Wolfe effect [7] (ISW), along with its nonlinear counterpart the Rees-Sciama effect [8] (RS), can provide a means to explore both of these open issues. This is because the ISWRS effect consists of the temperature variation experienced by Cosmic Microwave Background (CMB) photons [9] when passing through a time-varying gravitational potential Φ . In the linear regime, we can observe a non-zero $\dot{\Phi}$ either because of the accelerated expansion of the Universe, mainly induced by DE [10–14] or modified gravity effects [15–18], or because of spatial curvature [19]. In the nonlinear regime, Φ evolves primarily because of structure formation, and this is where neutrinos play a significant role. The presence of massive neutrinos induces in fact a slow decay of the gravitational potential [20] that generates ISWRS even in the absence of a background expansion. Therefore, a full reconstruction of the ISWRS effect could provide new insight into the physics of DE and neutrinos, aiding in the constraints on the DE Equation of State (EoS) and on the total neutrino mass M_ν .

The ISWRS signal is, however, exceedingly faint if compared to the primary anisotropies of the CMB, and direct measurements have yet to be achieved. However, we can reconstruct this signal by exploiting its cross-correlation with cosmological probes that trace the gravitational potential, whose variations induce the ISWRS effect itself [11, 21–27]. Moreover, these correlations are strongly influenced by the presence of massive neutrinos [28–31], making their detection a potential avenue for addressing questions on M_ν . Although cross-correlation with Φ -tracers improves the chances of detection by helping isolate the ISWRS signal that would otherwise be buried in primary CMB anisotropies, foregrounds, and noise, it comes at the cost of adding the associated complexities of the Φ -tracers to those of the CMB observations. The former generation of CMB experiments and Large Scale Structure (LSS) surveys has not been able to fully overcome the main obstacles that characterise this detection: cosmic variance limit, extragalactic foregrounds in CMB anisotropy maps, and the lack of data in the nonlinear regime, which is where neutrinos effects appear. However, ongoing advancements in CMB delensing [32] and foreground removal techniques (e.g. [33–36]) for CMB anisotropy maps, the implementation of analytical techniques to maximise the cross-correlation between CMB and LSS tracers (as studied in [37]), combined with high-sensitivity and high-resolution measurements by upcoming experiments, can pave the way not only for the detection of the ISWRS effect but also, in principle, for distinguishing between different M_ν values.

In this work, we forecast the feasibility of both these achievements via the combination of current and next-generation CMB experiments, the Simons Observatory (SO) [38, 39], a CMB-S4-like experiment [40, 41], CMB-HD [42, 43] and the space mission PICO [44, 45], with current LSS surveys, such as Euclid [46] and the Vera Rubin Observatory (hereafter, LSST) [47, 48]. To perform this analysis we exploit the analytical method developed in [31], to compute the cross-angular power spectra between the ISWRS effect and three Φ -tracer probes: galaxy clustering (GC), cosmic shear (CS) and CMB-lensing potential (CMBL). Because of the different effect that different values of M_ν have on the cross-spectra, we explore five $\nu\Lambda$ CDM cosmologies in our analysis, using as baseline the Planck 2018 one [4]. These studies are particularly relevant not only to produce forecasts for the considered ongoing and forthcoming experiments, but also because testing diverse experiments (i.e., ground-based and satellites) and under different conditions (i.e., different levels of delensing and foreground cleaning) enables to identify the optimal conditions for successfully detecting the ISWRS and, potentially, constraining M_ν in the future.

This paper is organised as follows. In Section 2 we summarise the theoretical framework for the ISWRS effect and its cross-correlation with tracers of the gravitational potential in the presence of massive neutrinos. In Section 3 we present our findings on the detectability of the ISWRS effect through its cross-correlation with Φ tracers, for both ideal conditions and realistic scenarios. Additionally, we assess the potential of distinguishing between different $\nu\Lambda$ CDM models through this detection. Finally, in Section 4 we draw our conclusions.

2 Theoretical Framework

2.1 Integrated Sachs Wolfe and Rees Scrima Effects

As a secondary anisotropy of the CMB, the ISW effect consists of a temperature variation that CMB photons undergo along their path from the last scattering surface to us. This temperature variation arises from the energy shift experienced by photons as they traverse time-varying gravitational potentials. We can retrieve this effect via the integration of the

time derivative of Φ over the whole propagation path [11]:

$$\frac{\Delta T_{\text{ISWRS}}}{T}(\hat{\mathbf{n}}) = -2 \int dz \frac{d\Phi(\hat{\mathbf{n}}, z)}{dz}, \quad (2.1)$$

where $\hat{\mathbf{n}}$ is a unit direction vector on the sphere, T is CMB temperature, Φ is the gravitational potential obtained from the Poisson equation, and we assume the visibility function of the photons $e^{-\tau(z)} \approx 1$ [49].

As anticipated, together with DE, another main responsible for the production of a not-vanishing time-derivative of the gravitational potential is the presence of massive neutrinos. This is because, after becoming non-relativistic, neutrinos free-stream with large thermal velocities that suppress the growth of density perturbations on scales smaller than the so-called “free-streaming length” [2, 26]:

$$\lambda_{\text{FS}}(z, m_\nu) \simeq 8.1 \frac{H_0(1+z)}{H(z)} \frac{1 \text{ eV}}{m_\nu} h^{-1} \text{Mpc}, \quad (2.2)$$

where m_ν is the mass of the single neutrino species (i.e. ν_e, ν_μ or ν_τ), $H(z)$ is the Hubble parameter as a function of the redshift z , that gives a measure of the expansion rate of the Universe, and $H_0 \equiv H(z=0)$ is the Hubble constant. Moreover, because of the gravitational back-reaction effects, the evolution of cold dark matter (CDM) and baryon densities is affected as well by the presence of neutrinos, and the total matter power spectrum is suppressed at scales $\lambda \ll \lambda_{\text{FS}}$ [50]. Consequently, on small cosmological scales, the free-streaming of neutrinos induces a slow decay of the gravitational potential, acting during both the matter and the DE dominated eras. This effect depends on the total neutrino mass M_ν . The more neutrinos are massive, the more the matter power spectrum will be suppressed with respect to the massless neutrino case, and therefore nonlinearities will appear on smaller scales.

In the angular power spectrum of the ISWRS effect, this suppression translates into a decrease with respect to the massless scenario, and this decrease intensifies as the neutrino mass increases [30, 31].

2.2 Cross-correlation with matter tracers in the presence of massive neutrinos

Despite its significant potential to uncover a multitude of insights, the ISWRS effect remains challenging to measure because it is extremely faint compared to CMB primary anisotropies. However, Crittenden and Turok (1996) [21] showed that it could be detected through the cross-correlation of the CMB with a local tracer of the mass. This is because LSS probes trace the same gravitational potential whose variation induces the ISWRS effect [11, 22–27]. In this work, we focus on galaxy clustering (GC), cosmic shear (CS), and CMB-lensing potential (CMBL).

Reconstructing the ISWRS effect via its cross-correlation with these probes is possible because they live in the same Universe era in which the ISWRS effect is generated. This means that the window functions of these fields, which represent their evolution in time, overlap, as shown in Figure 1. The LSS probes window functions can be computed as [51–55]:

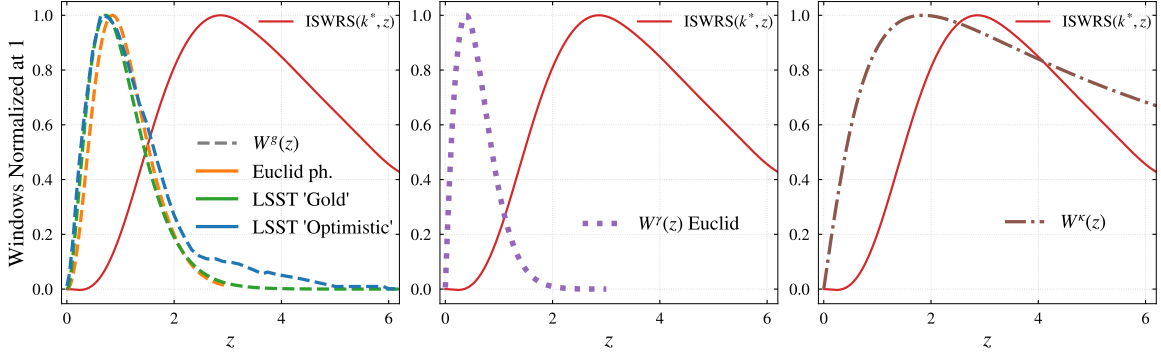


Figure 1: Time evolution functions of the investigated fields. The solid red lines in the three panels represent the ISWRS response as a function of z computed at a scale $k^* = (\ell^* + 1/2)/\chi(z)$, where $\ell^* = 5000$. (This specific scale has been chosen since it represents the range of nonlinear scales that mainly contribute to the cumulative S/N .) The left panel shows the window function of the Euclid photometric GC sample (dashed orange line), of the LSST “Gold” (dashed green line) and the LSST “Optimistic” GC samples (dashed blue line). The central panel represents the CS window function of the Euclid photometric survey (dotted purple line). Finally, the CMB lensing convergence window function is represented in the right panel (dot-dashed brown line).

$$W^g(z) = \frac{n(z)}{\bar{n}} b(z), \quad (2.3a)$$

$$W^\gamma(z) = \frac{3}{2} \frac{H_0^2}{c H(z)} \Omega_m \frac{\chi(z)}{a(z)} \frac{1}{\bar{n}} \int_z^{z_{\max}} dz' n(z') \frac{\chi(z') - \chi(z)}{\chi(z')}, \quad (2.3b)$$

$$W^\kappa(z) = \frac{3}{2} \frac{H_0^2}{c H(z)} \Omega_m \frac{\chi(z)}{a(z)} \frac{\chi(z_{ls}) - \chi(z)}{\chi(z_{ls})}, \quad (2.3c)$$

where $n(z)$ is the galaxy number density as a function of redshift; $b(z)$ is the galaxy bias function; $a(z)$ is the Universe scale factor; Ω_m is the parameter of matter density today; $\chi(z)$ is the comoving distance; $z_{ls} = 1100$ is the redshift at the last-scattering surface and:

$$\bar{n} = \int_{z_{\min}}^{z_{\max}} dz n(z).$$

Equations (2.3a) and (2.3b) represent the window functions for the galaxy distribution (g) and shear (γ), while Equation (2.3c) is the convergence (κ) window function, that can be converted into CMBL potential via Poisson’s equation in harmonic space:

$$\kappa_{\ell m} = \frac{\ell(\ell+1)}{2} \Phi_{\ell m}. \quad (2.4)$$

The time evolution of the ISWRS can be instead directly retrieved from the derivative of the Poisson’s equation [28]:

$$\dot{\Phi}(k, t) = -\frac{3}{2} \Omega_m \left(\frac{H_0}{c k} \right)^2 \partial_t \left[\frac{\delta(k, t)}{a(t)} \right]. \quad (2.5)$$

We explicitly assume a flat Universe. The larger the overlap between the probes time evolution function, the higher their cross-spectrum is expected to be, and consequently the probability of detecting the ISWRS signal is increased. This is because the cross-spectrum depends on the LSS windows product with the ISWRS as follows:

$$C_\ell^{\dot{\Phi}Y} = -2 \int dz \frac{H(z)}{c\chi^2(z)} W_Y(z) P_{\dot{\Phi},\delta}(k, z), \quad (2.6)$$

where the $P_{\dot{\Phi}\delta}(k, z)$ power spectrum arises after the window functions are multiplied by the $\delta(k, z)$ function and the relation $\langle \dot{\Phi}(k, z), \delta(k, z) \rangle \equiv P_{\dot{\Phi}\delta}(k, z)$ is used. The Y field is one of the Φ -tracer probes (g, γ, Φ), and we get respectively [26, 31, 37, 53, 56]:

$$C_\ell^{\dot{\Phi}g} = \frac{3\Omega_m H_0^2}{2c^3(\ell + 1/2)^2} \int_{z_{\min}}^{z_{\max}} dz H(z) \frac{n(z)}{\bar{n}} b(z) a(z) \left[\partial_z \frac{P_{\delta\delta}(k = \frac{\ell+1/2}{\chi(z)}, z)}{a^2(z)} \right], \quad (2.7a)$$

$$C_\ell^{\dot{\Phi}\gamma} = \left[\frac{3\Omega_m H_0^2}{2(\ell + 1/2)c^2} \right]^2 \int_{z_{\min}}^{z_{\max}} dz \left[\partial_z \frac{P_{\delta\delta}(k = \frac{\ell+1/2}{\chi(z)}, z)}{a^2(z)} \right] \times \frac{\chi(z)}{\bar{n}} \int_z^{z_{\max}} dz' n(z') \frac{\chi(z') - \chi(z)}{\chi(z')}, \quad (2.7b)$$

$$C_\ell^{\dot{\Phi}\Phi} = 2 \left[\frac{3\Omega_m H_0^2}{2(\ell + 1/2)^2 c^2} \right]^2 \int_{z_{\min}}^{z_{\max}} dz \chi(z) \frac{\chi(z_{ls}) - \chi(z)}{\chi(z_{ls})} \left[\partial_z \frac{P_{\delta\delta}(k = \frac{\ell+1/2}{\chi(z)}, z)}{a^2(z)} \right], \quad (2.7c)$$

where k is in Limber approximation [57]:

$$k_{\text{Limber}} = \frac{\ell + 1/2}{\chi(z)}, \quad (2.8)$$

and the derivation of $\partial_z P_{\delta\delta}(k, z)$ is detailed in Appendix B. Moreover, in Equation (2.7c), the following approximation has been used for Equation (2.4):

$$\Phi_{\ell m} \simeq \frac{2}{(\ell + 1/2)^2} \kappa_{\ell m}, \quad (2.9)$$

valid since we are focussing on very small scales (i.e. very large ℓ) in this work.

The curves of Figure 2 represent the absolute value of Equations (2.7), from left to right. To realise them, and all the results shown in this work, we use as a baseline the Planck 2018 cosmology (parameters from the last column of Table 2 of [4]), namely a flat Λ CDM model with $M_\nu = 0.06$ eV generalised by varying only the sum of the neutrino masses over the values $M_\nu = [0.0, 0.06, 0.12, 0.18, 0.24, 0.30]$ eV, whence the corresponding values of Ω_ν and Ω_{cdm} , keeping fixed Ω_m and Ω_b . The galaxy selection and bias functions are those of the Euclid photometric survey, given respectively by [51, 58]:

$$n_{\text{Euclid}}(z) \propto \left(\frac{z}{z_0} \right)^2 \exp \left[- \left(\frac{z}{z_0} \right)^{3/2} \right], \quad (2.10a)$$

$$b_{\text{Euclid}}(z) = A + \frac{B}{1 + \exp[-(z - D)C]}, \quad (2.10b)$$

with $z_0 = 0.9/\sqrt{2}$, $A = 1.0$, $B = 2.5$, $C = 2.8$, $D = 1.6$, and mean galaxy number density of $\bar{n} = 30 \text{ arcmin}^{-2}$.

Additionally, in this work, we test the galaxy selection and bias functions of the LSST survey [47, 48] (see left panel of Figure 1):

$$n_{\text{LSST}}(z) \propto \frac{1}{2z_0} \left(\frac{z}{z_0} \right)^2 \exp \left[- \left(\frac{z}{z_0} \right) \right], \quad (2.11a)$$

$$b_{\text{LSST}}(z) = 0.95(1+z), \quad (2.11b)$$

where $z_0 = 0.3$. These functions refer to the LSST “Gold” sample, where with the term “Gold” we consider the $i < 25$ magnitude sample, with $\bar{n} = 40 \text{ arcmin}^{-2}$ [47]. We consider even a more “Optimistic” LSST sample corresponding to $i < 27$ [59], which includes Lyman break galaxies from redshift dropouts, which results in an increase of the number density of galaxies to $\bar{n} = 66 \text{ arcmin}^{-2}$ [37, 60, 61].

All the other terms in Equations (2.7) have been computed using **CAMB**¹ [62], setting Takahashi as **Halofit** model [63, 64], that includes Bird’s² corrections for neutrinos masses [65]. The choice to use this nonlinear model follows from our previous work [31], where we validated Equations (2.7a) and (2.7c) against the cross-spectra extracted from the “Dark Energy and Massive Neutrino Universe” (DEMNUni) N-body numerical simulations [30, 66–76], and verified that the Takahashi modelling works better if compared with the Mead2020 model [77] for these analytical reconstructions. For the validation of Equation (2.7b), see Appendix A.

The cross-spectra shown in Figure 2 are characterised by the presence of a sign inversion that appears in correspondence with the transition from the linear to the nonlinear regime, due to the anti-correlation between RS and the Φ tracers (i.e. $\langle \Phi \dot{\Phi} \rangle > 0$ in the late-time ISW regime, and $\langle \Phi \dot{\Phi} \rangle < 0$ in the RS regime [29, 78]). Moreover, the presence of massive neutrinos affects these cross-angular power spectra. In fact, as neutrino mass increases, nonlinearities appear on smaller cosmological scales and the sign inversion appears on larger multipoles [30, 31]. From the subpanels of Figure 2 it is in fact clear that the more neutrinos are massive, the more the sign inversion shifts towards smaller cosmological scales, and the dependency is almost linear [31].

3 Detectability of the ISWRS effect and identification of $\nu\Lambda\text{DM}$ model

As previously mentioned, properly reconstructing the ISWRS effect via its cross-correlation with GC, CS and CMBL is possible because these probes trace the variation of the gravitational potential that induces the ISWRS itself. Since the amplitude of the LSS and ISWRS cross-angular power spectra directly depends on the overlap between their window functions, the larger the overlap, the greater their cross-spectrum is expected to be. The straightforward consequence is an increased probability of detecting the ISWRS signal.

The significance of the detection can be quantified by the cumulative signal-to-noise ratio (S/N), where the signal is the cross-power spectrum $C_\ell^{\Phi Y}$ (with Y one of the Φ tracers: g, γ ,

¹<https://CAMB.readthedocs.io/en/latest/>

²As reported in the Readme of the **CAMB** webpage, on March 2014 modified massive neutrino parameters were implemented in the nonlinear fitting of the total matter power spectrum to improve the accuracy of the updated **Halofit** version from [64]. These fitting parameters, accounting for nonlinear corrections in the presence of massive neutrinos, are different from the ones implemented by [65] in the original **Halofit** version from [63].

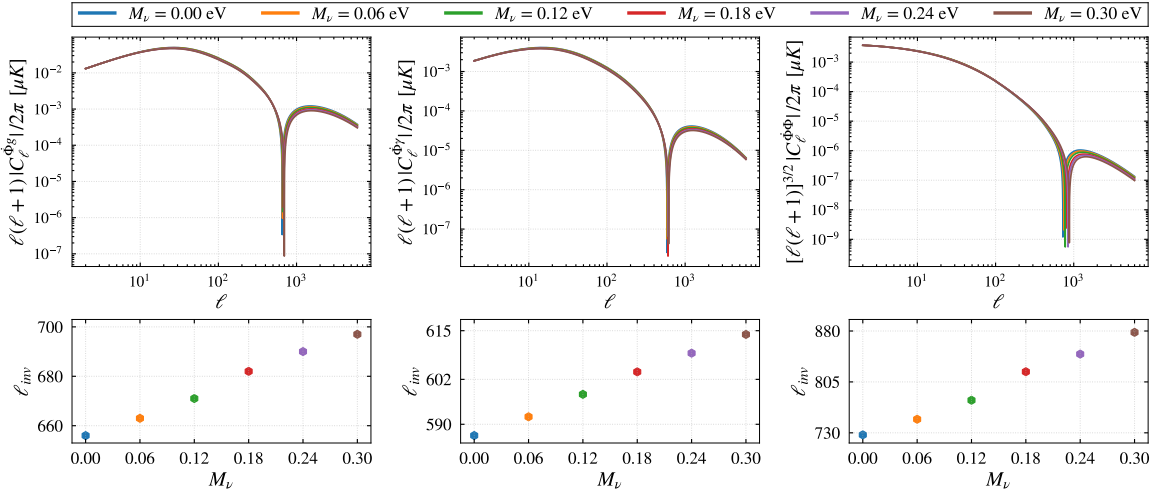


Figure 2: Analytical predictions for the cross-correlation between the ISWRS effect and GC, CS and CMBL, from left to right, computed for $\nu\Lambda\text{CDM}$ models with five different values of the total neutrino mass: $M_\nu = 0.06$ eV (orange), 0.12 eV (green), 0.18 eV (red), 0.24 eV (purple), 0.30 eV (brown). Together with them, the results for the massless case have been reported (blue). As GC and CS probes, the Euclid photometric sample has been used [51]. The upper panels represent the absolute value of the three angular cross-power spectra. The lower ones show how the position of the characteristic sign inversion varies with the value of M_ν .

Φ), and the associated uncertainty is given by:

$$\sigma_\ell^2 = \frac{(C_\ell^{TT} + d_\ell)(C_\ell^{YY} + N_\ell^Y) + (C_\ell^{\dot{\Phi}Y})^2}{(2\ell + 1) f_{sky}}, \quad (3.1)$$

resulting in [37, 49]:

$$\text{CUM.} \left(\frac{S}{N} \right) (\ell_{\max}) = \sqrt{f_{sky} \sum_{\ell=\ell_{\min}}^{\ell_{\max}} \frac{(2\ell + 1) (C_\ell^{\dot{\Phi}Y})^2}{(C_\ell^{TT} + d_\ell)(C_\ell^{YY} + N_\ell^Y) + (C_\ell^{\dot{\Phi}Y})^2}}, \quad (3.2)$$

where f_{sky} is the sky fraction covered by the overlap of the CMB experiment and LSS survey, C_ℓ^{TT} is the lensed primary CMB power spectrum, d_ℓ is the CMB detector noise (to which foreground residuals can be added), N_ℓ^Y is the noise associated to the Y probe.

Because of the different impact that different values of M_ν have at very small scales on the cross-spectra between the ISWRS effect and the three analysed probes (shown in the lower panel of Figure 2), a high significance detection for these correlations can in principle even allow to disentangle different $\nu\Lambda\text{CDM}$ models. We can, in fact, quantify the detectability, in units of σ , of a signal where $M_\nu > 0$ with respect to the massless case, via:

$$\sqrt{\chi^2}(\ell_{\max}) = \sqrt{\sum_{\ell=\ell_{\min}}^{\ell_{\max}} \frac{[C_\ell^{\dot{\Phi}Y}(M_\nu = 0.0 \text{ eV}) - C_\ell^{\dot{\Phi}Y}(M_\nu > 0.0 \text{ eV})]^2}{\sigma_\ell^2(M_\nu = 0.0 \text{ eV})}}. \quad (3.3)$$

In this work, $\ell_{\min} = 2$, $\ell_{\max} = 6000$ [37], $C_{\ell}^{\dot{\Phi}Y}$ has been computed with Equations (2.7), C_{ℓ}^{TT} has been extracted from **CAMB** and C_{ℓ}^{YY} has been computed analytically as [52]:

$$C_{\ell}^{YY} = \int dz \frac{H(z)}{c\chi^2(z)} [W^Y(k, z)]^2 P_{\delta\delta}(k, z). \quad (3.4)$$

which is Equation (2.6) in the case of $X = Y$.

3.1 Ideal forecasts

Despite the significant overlap between the window functions shown in Figure 1 which makes these cross-correlation signals particularly robust, the current CMB and LSS surveys are characterised by levels of statistical and instrumental noises that, together with the presence of foreground contamination, make the detectability of the ISWRS challenging, and the possibility of disentangling between different $\nu\Lambda$ CDM models likely unfeasible [31].

Ideally, the best detection (i.e., the highest S/N) would be possible if the Y probe window function perfectly overlaps with the ISWRS one, so that $C_{\ell}^{\dot{\Phi}Y} \equiv C_{\ell}^{\dot{\Phi}\dot{\Phi}}$, the survey is full-sky ($f_{sky} \simeq 1$), and the statistical and instrumental noises are negligible.

In such a case, Equation (3.2) becomes [37]:

$$\text{CUM.} \left(\frac{S}{N} \right)_{\text{ideal}} (\ell_{\max}) = \sqrt{\sum_{\ell=\ell_{\min}}^{\ell_{\max}} \frac{(2\ell+1)(C_{\ell}^{\dot{\Phi}\dot{\Phi}})^2}{(C_{\ell}^{TT} \cdot C_{\ell}^{\dot{\Phi}\dot{\Phi}}) + (C_{\ell}^{\dot{\Phi}\dot{\Phi}})^2}}. \quad (3.5)$$

Differently from the other auto-power spectra used in this work, $C_{\ell}^{\dot{\Phi}\dot{\Phi}}$ cannot be computed using Equation (3.4) without a proper treatment of nonlinearities. This is because the current status of Halofit models [63] in Boltzmann solver codes like **CAMB** is not advanced enough to accurately reconstruct $P_{\dot{\Phi}\dot{\Phi}}(k, z)$ (see Appendix B) in the nonlinear regime. To properly compute the ISWRS spectrum, including corrections due to nonlinearly evolved potentials, one needs to perform an expansion of the dark matter power spectrum $P_{\delta\delta}(k, z)$ using perturbation theory methods [53, 79], or to fit the $P_{\delta\delta}(k, z)$ model to N-body simulations [28], or to directly use the result of N-body simulations, as we show in this work.

Here we use the ISWRS auto-power spectra extracted from the DEMNUni maps [30] realised in the redshift range $z = [0.02, 7]$ for the baseline Planck Collaboration (2014b) cosmology [80], generalised to three $\nu\Lambda$ CDM cosmologies with $M_{\nu} = 0.0, 0.17, 0.30$ eV.

As shown in Figure 3, when using Equation (3.4) with $P_{\delta\delta}(k, z)$ computed with **CAMB**, as done in previous work [37], we are unable to properly recover nonlinear scales, underestimating the signal by more than 2 orders of magnitude.

In what follows, we therefore use the $C_{\ell}^{\dot{\Phi}\dot{\Phi}}$ extracted from DEMNUni maps in Equation (3.5) to estimate the maximum achievable S/N ratio. We consider both the cases of lensed and delensed C_{ℓ}^{TT} [32], and assess the possibility of disentangling different values of M_{ν} with Equation (3.3).

As shown in the left panel of Figure 4, a signal-to-noise ~ 200 is found, which can increase up to $\gtrsim 500$ if delensing techniques are applied to the CMB anisotropy data. In these conditions, it would be possible to identify the $\nu\Lambda$ CDM model. The ability to distinguish it from the massless case ranges from approximately 30σ for $M_{\nu} = 0.17$ eV without delensing, to about 140σ for $M_{\nu} = 0.30$ eV with delensed CMB, as shown in the right panel of Figure 4. To emphasise that the trend does not follow a specific linear growth law, in the right panel of Figure 4 we even show the result for $M_{\nu} = 0.53$ eV, made possible by the availability of the DEMNUni suite.

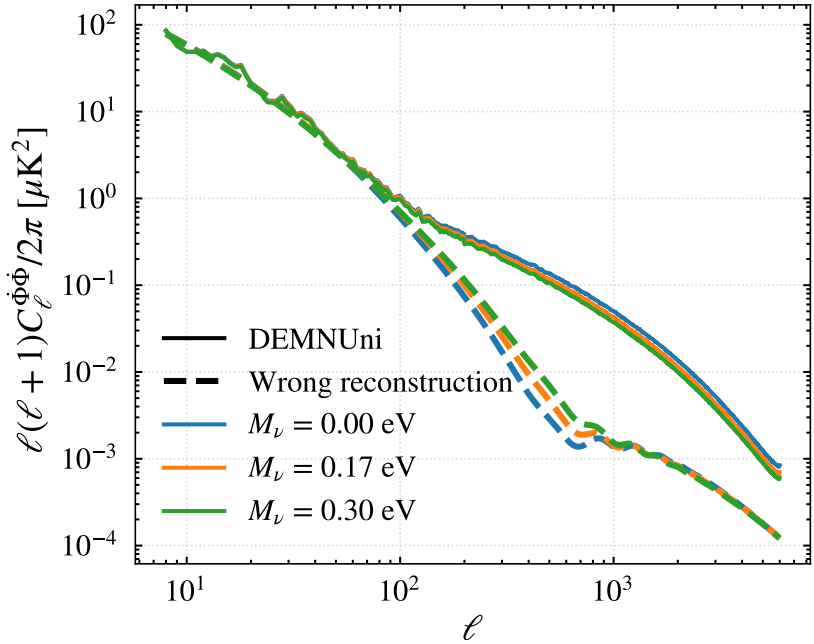


Figure 3: Comparison between the ISWRS angular auto-spectra extracted from DEMNUni simulations in the range $z = [0.02, 7]$ (solid lines) and those wrongly analytically computed (dashed lines), for three M_ν values: 0.0 eV (blue), 0.17 eV (orange), 0.30 eV (green).

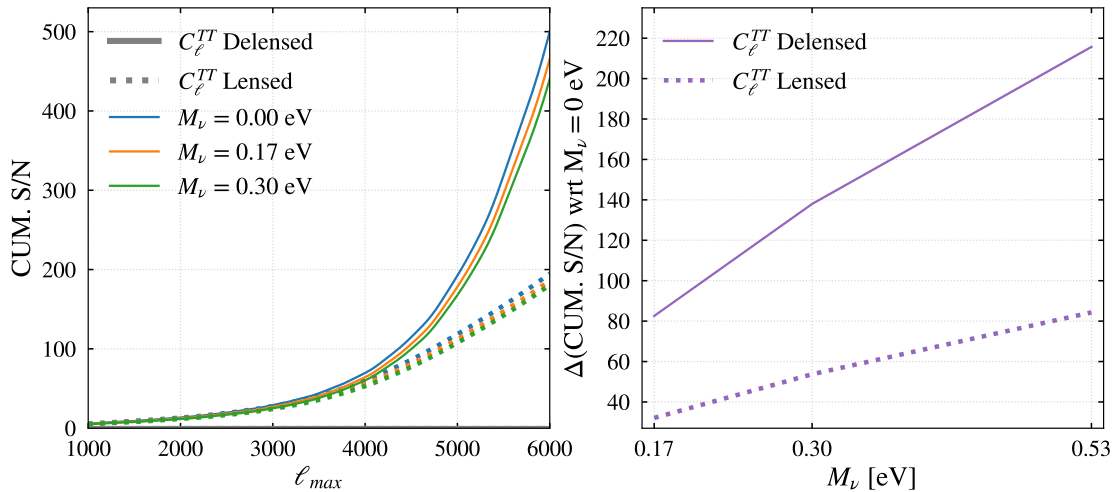


Figure 4: The left panel represents the results of the cumulative signal-to-noise ratio (CUM. S/N) obtained using Equation (3.5) with the $C_\ell^{\dot{\Phi}\dot{\Phi}}$ extracted from DEMNUni maps with $M_\nu = 0.0$ eV (blue), 0.17 eV (orange), 0.30 eV (green). The right panel shows the results for the identification of the $\nu\Lambda$ CDM model with respect to the massless case, obtained using Equation (3.3). We also add the result for the $\nu\Lambda$ CDM cosmology with $M_\nu = 0.53$ eV to show the actual increasing trend as the neutrino mass increases. Both panels present the results obtained with lensed (solid lines) and delensed (dotted lines) C_ℓ^{TT} .

3.2 Realistic forecasts for future CMB Experiments and LSS Surveys

Although the ideal case is certainly promising, the reality remains more challenging. This is because current state-of-the-art CMB and LSS experiments do not provide full-sky coverage and negligible noise effects. Not to mention the presence of foregrounds.

For our analysis, we consider several LSS and CMB surveys: the Euclid photometric survey [46, 51] and LSST “Gold” and “Optimistic” samples [47, 48, 59] as GC probes; the Euclid photometric survey as CS probe; SO [38], CMB-S4 [81], CMB-HD [42, 43, 82] and PICO [44, 45] as CMB experiments for CMBL and CMB-temperature. The specifications for the four CMB experiments considered are listed in Table 1, Table 2, Table 3 and Table 4.

In our realistic analysis, we test 5 ν ACDM models obtained from the baseline Planck 2018 cosmology [4], generalised assuming 5 different M_ν values: 0.06, 0.12, 0.18, 0.24, 0.30 eV. We consider three scenarios of increasing complexity, taking into account the impact of CMB primary anisotropies, detector noise, and residual foregrounds:

- **Delen.** + **D.N.** : delensed C_ℓ^{TT} + detector noise;
- **Len.** + **D.N.** : lensed C_ℓ^{TT} + detector noise;
- **Len.** + **ILC** : lensed C_ℓ^{TT} + detector noise + residual foreground.

Frequency (GHz)	27	39	93	145	225	280
FWHM (arcmin)	7.4	5.1	2.2	1.4	1.0	0.9
TT noise (μ K-arcmin)	71	36	8.0	10	22	54

Table 1: Experimental assumptions for SO.

Frequency (GHz)	20	27	39	93	145	225	280
FWHM (arcmin)	10.0	7.4	5.1	2.2	1.4	1.0	0.9
TT noise (μ K-arcmin)	45.9	15.5	8.7	1.5	1.5	4.8	11.5

Table 2: Experimental assumptions for CMB-S4.

Frequency (GHz)	30	40	90	150	220	280
FWHM (arcmin)	1.30	0.94	0.41	0.25	0.17	0.13
TT noise (μ K-arcmin)	6.50	3.40	0.73	0.79	2.00	4.60

Table 3: Experimental assumptions for CMB-HD.

For the first two scenarios, the noise sensitivities of the different frequency channels are combined using an inverse-variance weighting, after convolution with the corresponding Gaussian beam window functions [83]:

$$d_\ell = \left[\sum_\nu \frac{1}{d_{\nu\ell}} \right]^{-1}. \quad (3.6)$$

Frequency (GHz)	21	25	30	36	43	52	62	75	90	108
FWHM (arcmin)	38.4	32.0	28.3	23.6	22.2	18.4	12.8	10.7	9.5	7.9
TT noise ($\mu\text{K-arcmin}$)	23.9	18.4	12.4	7.9	7.9	5.7	5.4	4.2	2.8	2.3

Frequency (GHz)	129	155	186	223	268	321	385	426	555	666	788
FWHM (arcmin)	7.4	6.2	4.3	3.6	3.2	2.6	2.5	2.1	1.5	1.3	1.1
TT noise ($\mu\text{K-arcmin}$)	2.1	1.8	4.0	4.5	3.1	4.2	4.5	9.1	45.8	177	1050

Table 4: Experimental assumptions for PICO (baseline).

with

$$d_{\nu \ell} = \Delta_{T \nu}^2 \exp \left[\frac{\theta_{FWHM \nu}^2 \ell^2}{8 \ln 2} \right]. \quad (3.7)$$

where $\Delta_{T \nu}$ is the noise level of the experiment (third row of Tables 1, 2, 3, 4) and $\theta_{FWHM \nu}$ is the full-width at half-maximum of a Gaussian beam (second row of Tables 1, 2, 3, 4).

For the third scenario, we use the Internal Linear Combination method [84], and specifically the one implemented in the `BasicILC` code³, to optimally combine the different frequency channels, minimizing the contribution of noise and foregrounds. We account for the expected small-scale foregrounds at each frequency channel, specifically Sunyaev-Zel'dovich effects, Cosmic Infrared Background, and radio point sources. These components are modelled using the latest data from ground-based experiments such as the Atacama Cosmology Telescope (ACT, [85]) and the South Pole Telescope (SPT, [86]). In this respect, our analysis is to be considered conservative and bound to be improved thanks to future higher-resolution measurements, for which it will be possible to more efficiently resolve and mask sources. Throughout our cross-correlation studies, we make the starting point approximation that any residual foreground in CMB anisotropy maps does not correlate with the tracers of the LSS, even in the case of CMBL. Finally, for ground-based experiments like SO, CMB-S4 and CMB-HD, we do not attempt to model the impact of the Earth's atmosphere, which predominantly affects large scales.

In Equation (3.2), as noise for the gravitational potential tracers, N_ℓ , we use the shot-noise \bar{n}^{-1} for the GC probes as given in Section 2.2, the specific CMBL reconstruction noise for CMB-S4 [87], CMB-HD [82] and PICO [44] (see Figure 5), while for the CS probe we use [88]:

$$N_\ell^\gamma = \frac{\sigma_\epsilon^2}{2 \bar{n}}, \quad (3.8)$$

where σ_ϵ^2 is the variance of the intrinsic galaxy ellipticity, assumed to be 0.3 for the Euclid photometric survey [51].

Lastly, given the tested CMB and LSS experiments, we assume for our analysis the f_{sky} listed in Table 5, as the result of their overlap [37, 40, 43, 89, 90].

To represent the results of the application of Equation (3.2) and Equation (3.3) with all the aforementioned components, we use grouped bar charts. In the following Sections, Figures 7 - 12, for each cross-correlation investigated, the colour of the bars indicates the CMB

³<https://github.com/EmmanuelSchaan/BasicILC>

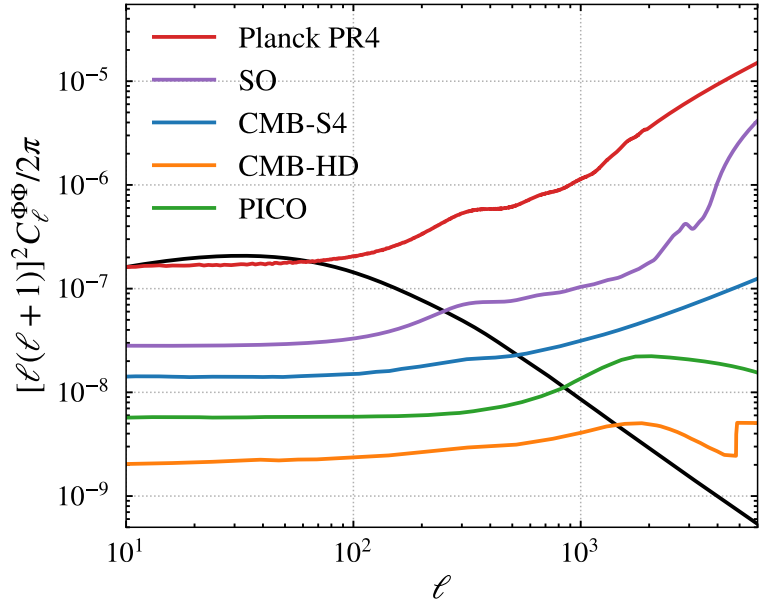


Figure 5: CMB-lensing potential reconstruction noise levels for the four CMB experiments tested: SO (purple), CMB-S4 (blue), CMB-HD (orange), PICO (green). The Planck PR4 (red) has been reported as a reference. In black the theoretical CMB lensing potential for the Planck cosmology.

	Euclid	LSST	SO	CMB-S4	CMB-HD	PICO
SO	0.25	0.40	0.40	/	/	/
CMB-S4	0.25	0.40	/	0.40	/	/
CMB-HD	0.25	0.40	/	/	0.50	/
PICO	0.36	0.40	/	/	/	0.90

Table 5: Overlapping sky fraction between each pair of experiments.

experiment simulated to represent the ISWRS effect (or both the ISWRS and the Φ -tracer in the case of the cross-correlation with CMBL). The shade of the colour indicates the M_ν model: we report the results for all the $\nu\Lambda$ CDM cosmologies analysed, from lighter shades that represent lighter M_ν , to darker that represent heavier models. The cumulative S/N (left panels) and the $\sqrt{\chi^2}$ (right panels) represented by the bars correspond to the values reached in correspondence of $\ell_{\max} = 6000$.

3.3 Galaxy clustering – Optimal Weighting

The cross-correlation between the ISWRS effect and GC is the most widely investigated, primarily because of the higher cross-angular power spectrum signal. Several techniques have also been developed to reshape the galaxy number count distribution in order to optimize the S/N [37, 91, 92]. For this cross-correlation only, in fact, together with the three scenarios listed in the previous Section, we consider even a fourth scenario. Following the example of

Ferraro et al. (2022) [37], we implement a method to improve the overlap between ISWRS and GC window functions and to maximise the S/N : the optimal weighting (O.W.).

O.W. We know that the majority of galaxy surveys are characterized by a large number of galaxies at low redshift ($z \sim 1$), but the peak of the ISWRS is at high redshift ($z \sim 2-4$). To maximise the overlap between the window functions, and consequently maximise the S/N , we can up-weight galaxies at higher redshift via the usage of [37]:

$$w(z) \propto \frac{b(z) W^{\dot{\Phi}}(k^*, z) P_{\delta\delta}(k^*, z)}{\left(\frac{n(z)}{\bar{n}}\right) \left[b^2(z) P_{\delta\delta}(k^*, z) + \frac{\chi^2}{H(z) n(z)}\right]}, \quad (3.9)$$

which is the expression of the O.W., where $k^* = \frac{\ell^* + 1/2}{\chi(z)}$, with $\ell^* = 5000$, as this is the scale from which most of the ISWRS signal comes from [37].

Transforming $W^g(k, z)$ into $w(k^*, z) \cdot W^g(k, z)$ increases the overlap between the window functions, as illustrated in Figure 6. This comes at the cost of increasing the shot-noise, because higher redshift galaxies are rare. It is converted from the usual \bar{n}^{-1} to [37, 91, 92]:

$$\frac{1}{\bar{n}_{O.W.}} = \frac{1}{\bar{n}^2} \int dz n(z) w^2(z). \quad (3.10)$$

However, since Equation (3.9) is the result of the minimisation of the noise via the Lagrangian multiplier, this construction allows to balance the shot-noise increase, as comprehensively explained in Appendix A of [37].

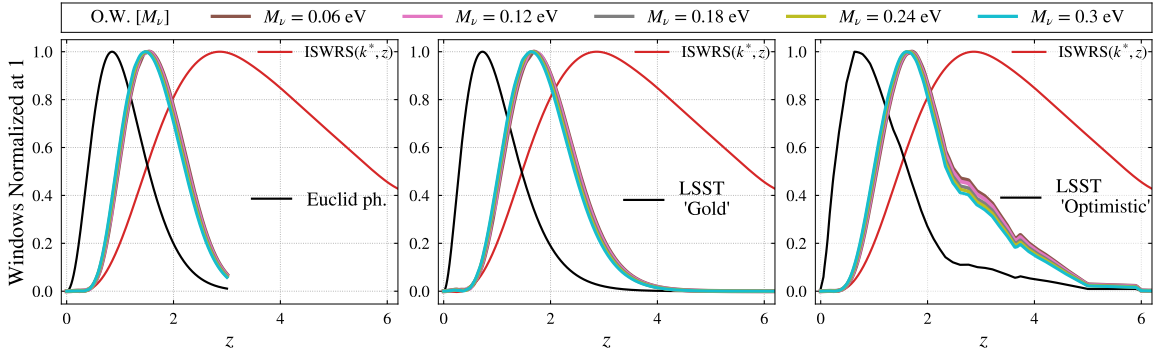


Figure 6: Window functions of the photometric Euclid, LSST “Gold” and LSST “Optimistic” GC samples from left to right (black solid lines), together with the ISWRS response as a function of z computed at a scale $k^* = (\ell^* + 1/2)/\chi(z)$, where $\ell^* = 5000$ (red lines). In each panel, the results for the application of the optimal weighting (O.W.) to each survey have been reported. Being the O.W. cosmology-dependent, we report the results obtained for each of the $\nu\Lambda$ CDM cosmologies tested, with $M_\nu = 0.0$ eV (cyan), 0.06 eV (brown), 0.12 eV (pink), 0.18 eV (grey), 0.24 eV (acid green), 0.30 eV (cyan).

As Equation (3.9) depends on $P_{\delta\delta}(k, z)$, we compute a specific $w(k^*, z)$ for each $\nu\Lambda$ CDM cosmology tested. This is the reason why in Figure 6 there is a different $w(k^*, z) W^g(k, z)$ for each M_ν value, showed for $k = k^*$.

3.3.1 Euclid photometric (GC) \times ISWRS

Figure 7 shows the results for the combination of the photometric Euclid GC survey with the four CMB experiments. In the left panel, we represent the cumulative S/N results from the application of Equation (3.2). A detection of the ISWRS effect appears feasible with next-generation CMB experiments, provided that foregrounds can be kept under control or that optimal weighting of the GC is efficiently applied. The highest detections are achieved when considering delensed C_ℓ^{TT} affected only by detector noise, particularly for the combination with CMB-HD, where we find an $\sim 11\sigma$ detection for $M_\nu = 0.06$ eV. The lowest S/N level occurs when considering lensed C_ℓ^{TT} combined with detector noise and foregrounds, especially in the case of the combination with SO where there is a $\sim 1.2\sigma$ detection for $M_\nu = 0.30$ eV. We want then to highlight the recovery achieved when applying the O.W. to the case of lensed $C_\ell^{TT} + \text{ILC}$. The improvement in the detection is of $\sim 38\%$ in the combination with SO, $\sim 41\%$ with CMB-S4, $\sim 42\%$ with CMB-HD and $\sim 39\%$ with PICO. In the right panel, we present the results from the application of Equation (3.3), which provides information on the ability to distinguish a specific $\nu\Lambda\text{CDM}$ model from the massless case. Only for CMB-HD, in the most optimistic conditions, there is the possibility to set constraints on the neutrino mass. Considering the current constraints on M_ν (< 0.11 eV 95% C.L.; [5]), this cross-correlation analysis, with these combinations of experiments, will not lead to new constraints on neutrino masses.

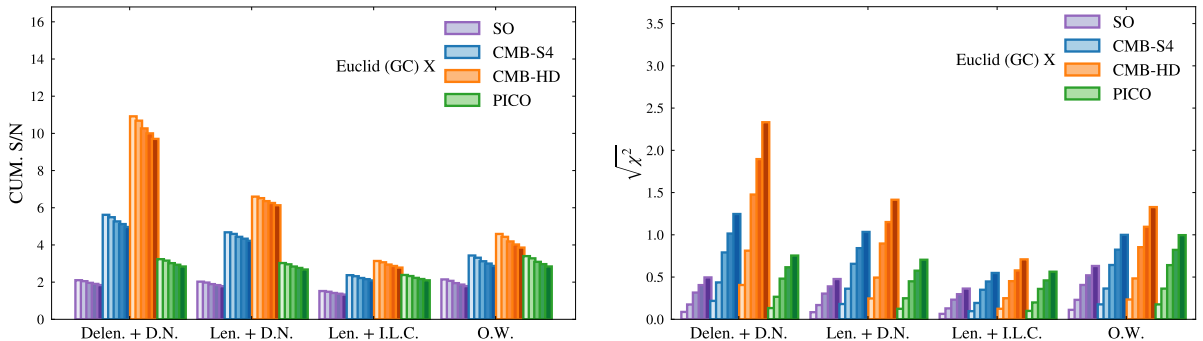


Figure 7: Results for the photometric Euclid GC survey cross-correlation with all the CMB experiments, for all the $\nu\Lambda\text{CDM}$ models analysed. For each of the four scenarios tested, the purple bars represent the results for the cross-correlation with SO, the blue bars for those with CMB-S4, the orange bars for those with CMB-HD and the green bars for those with PICO. For every combination of the Euclid (GC) survey with a CMB experiment, the results for all the 5 $\nu\Lambda\text{CDM}$ models have been represented with a bar (with M_ν increasing from 0.06 eV to 0.30 eV from left to right). The left panel shows the results of the cumulative S/N in correspondence of $\ell_{max} = 6000$ computed with Equation (3.2). The right one shows the possibility of distinguishing the $\nu\Lambda\text{CDM}$ model with respect to the massless case, computed with Equation (3.3).

3.3.2 LSST “Gold” (GC) \times ISWRS

Figure 8 shows the results for the combination of the LSST “Gold” sample with the four CMB experiments. In this case, the trend of the bars of the left panel is very similar to the one of Figure 7. However, because of the higher \bar{n} and the larger sky coverage overlap with the CMB experiments, the S/N levels achieved with the LSST “Gold” sample are overall higher.

Our results reach a maximum of $\sim 12\sigma$ for the combination with CMB-HD, when considering delensed C_ℓ^{TT} affected only by detector noise for $M_\nu = 0.06$ eV, and a minimum of $\sim 1.5\sigma$ in the combination with CMB-SO, when considering lensed C_ℓ^{TT} combined with detector noise and foreground for $M_\nu = 0.30$ eV. Even in this case, the large recovery when applying the O.W. is evident, with an increase of the S/N level of $\sim 69\%$ for the combination with SO, $\sim 73\%$ with CMB-S4, $\sim 75\%$ with CMB-HD and $\sim 71\%$ with PICO. The results in the right panel of Figure 8 confirm the improvement obtained with these combinations of experiments. Again the most promising results are obtained with CMB-HD, with some discriminating power at the 1.5σ level also for CMB-S4. Nevertheless, these promising results are achieved for M_ν values higher than 0.11 eV (95% C.L. [5]) and make also these combinations not constraining.

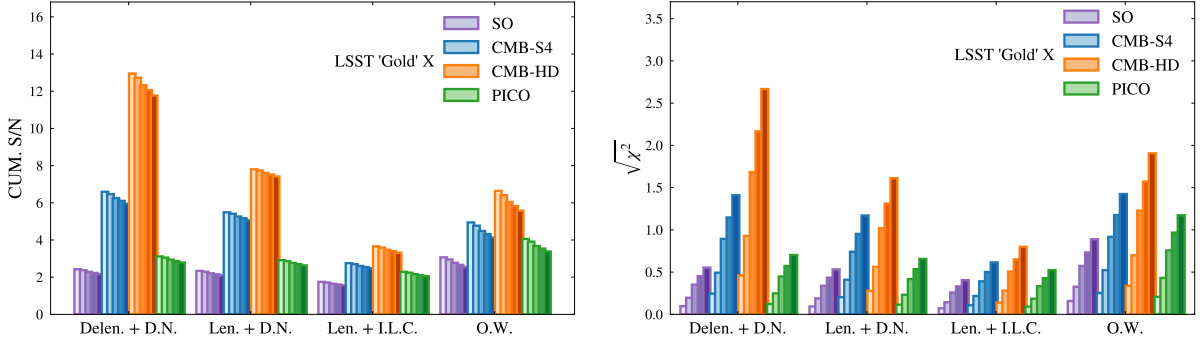


Figure 8: Same as Figure 7, but for the LSST “Gold” sample.

3.3.3 LSST “Optimistic” (GC) \times ISWRS

Figure 9 shows the best results achieved for the cross-correlation of GC with ISWRS, obtained from the combination of the LSST “Optimistic” sample with the four CMB experiments. This was expected from the superposition of the window functions (both with and without the O.W. application) shown in the right panel of Figure 6, and from the very high \bar{n} (i.e., very low shot-noise). Here not only a minimum of 2σ detection level is always guaranteed, but a 7σ detection level is reached for all the cosmologies tested, in the first, the second and the fourth scenarios, in combination with CMB-HD. Achieving this result for all the analysed $\nu\Lambda$ CDM cosmologies when applying the O.W. suggests the huge potential that this technique can have on real measurements in general, and on LSST ones in particular. Overall, the results achieved range from a maximum of $\sim 16\sigma$ detection for the combination with CMB-HD, when considering delensed C_ℓ^{TT} affected only by detector noise for $M_\nu = 0.06$ eV, and a minimum of $\sim 2\sigma$ detection in the combination with SO, when considering lensed C_ℓ^{TT} combined with detector noise and residual foregrounds for $M_\nu = 0.30$ eV. The recovery here when applying the O.W. is of $\sim 78\%$ in combination with SO, $\sim 83\%$ with CMB-S4, $\sim 85\%$ with CMB-HD and $\sim 81\%$ with PICO, certainly larger with respect to the previous cases. The results for the M_ν investigation are more interesting, as we reach $> 1\sigma$ detection level for $M_\nu = 0.12$ eV in combination with CMB-HD in the first scenario. Although the conditions of the first scenario are undoubtedly idealistic and not achievable in the near future, they make this cross-correlation, with this combination of experiments, a promising probe to infer tighter constraints on M_ν .

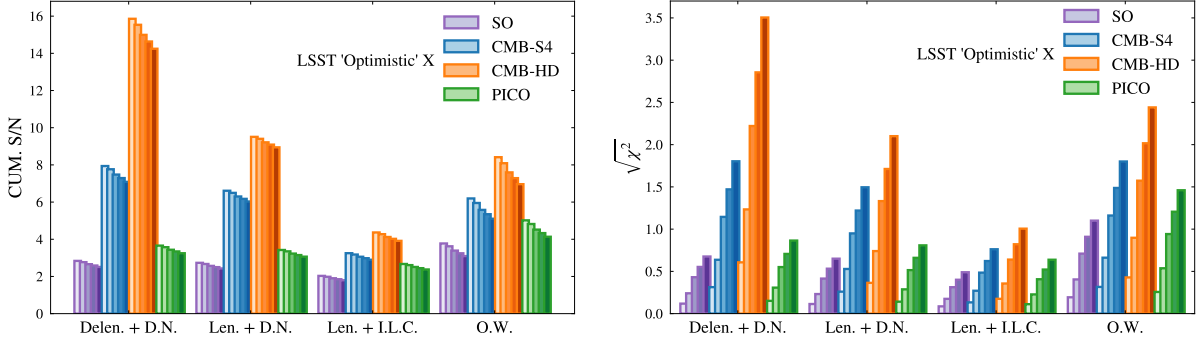


Figure 9: Same as Figure 7, but for the LSST “Optimistic” sample.

3.4 Cosmic Shear

The superposition between the window functions of CS and the ISWRS effect is significantly lower with respect to the case of GC (see Figure 1). This results in a lower signal for the cross-correlation of these two fields, as shown in the middle panel of Figure 2, that, together with a noise of the order of the GC one, makes this detection more challenging. Moreover, the analytical reconstruction of this cross-correlation is less precise when compared to the others, due to the greater sensitivity of the CS field to nonlinearities. Because of the assumptions made in the `Halofit` model, the analytical implementation does not provide a correct recovery of the amplitude of this cross-correlation in the nonlinear regime, and in particular underestimates the results of N-body simulations (see Appendix A), negatively impacting our analysis.

3.4.1 Euclid photometric (CS) \times ISWRS

Figure 10 shows the results for the combination of the photometric Euclid CS survey with the four CMB experiments. It is immediately evident that these results are the less promising findings of this work. A $\gtrsim 1\sigma$ level is reached only in the case of the combination with CMB-HD, in the first and most optimistic scenario, with all the $\nu\Lambda$ CDM cosmologies tested. The highest S/N level is achieved within this case and corresponds to $\sim 1.5\sigma$ for $M_\nu = 0.06$ eV. Not guaranteeing the detection, this cross-correlation does not provide any chance at all to identify the cosmological model, as shown in the right panel, where the results barely reach the 0.2σ level.

3.4.2 N-body simulation analysis

Since our analytical implementation does not provide a correct recovery of the amplitude of this cross-correlation, we perform a comparison between the detectability results obtained with our analytic implementation and those obtained using the spectra extracted from N-body simulations. Specifically, for the latter case, we use the cross-spectra extracted from a set of ISWRS and CS correlated DEMNUni maps, realised for the Planck 2014b cosmology [80], extended to the cases where $M_\nu = 0.0, 0.17, 0.30, 0.53$ eV, in the redshift range $z = [0.2, 2.5]$. The CS maps have been produced using the techniques described in [93–95], assuming the galaxy distribution given by Equation (2.10a). For a proper comparison, the same cosmologies and redshift range have been adopted to reassess our analytical results.

It is clear from Figure 11 that using the results of N-body simulations significantly improves the S/N ratio, leading to a maximum of 6.5σ for the $M_\nu = 0.6$ eV $\nu\Lambda$ CDM cosmology, in

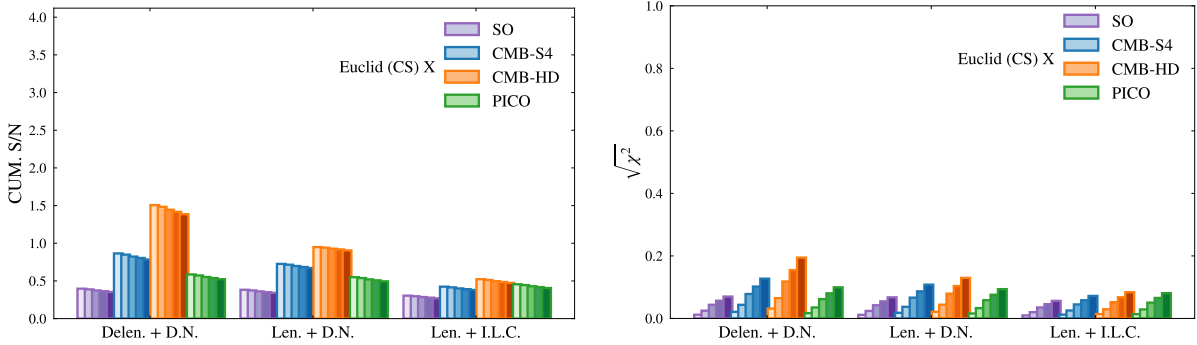


Figure 10: Same as Figure 7, but for the Euclid photometric CS combined with the four CMB experiments, for the three scenarios tested in this case.

the case of the combination with CMB-HD for delensed C_ℓ^{TT} assuming only detector noise, and to a minimum level of $\sim 0.3\sigma$ in combination with SO, when considering lensed C_ℓ^{TT} with detector noise and foregrounds for $M_\nu = 0.30$ eV. These same configurations computed analytically result in a S/N level that ranges from a maximum of $\sim 1.6\sigma$ in the combination with CMB-HD for delensed C_ℓ^{TT} assuming only detector noise, to a minimum of $\sim 0.2\sigma$ in the combination with SO, when considering lensed C_ℓ^{TT} with both detector noise and foregrounds for $M_\nu = 0.30$ eV. Accordingly to the improvement in the detection level, the possibility to disentangle the M_ν value is restored when using N-body simulations, whence a $\gtrsim 1\sigma$ level is reached with: CMB-S4 in the first (for $M_\nu = 0.17, 0.30, 0.53$ eV) and in the second (for $M_\nu = 0.30, 0.53$ eV) scenarios; CMB-HD in the first (for $M_\nu = 0.17, 0.30, 0.53$ eV), the second (for $M_\nu = 0.17, 0.30, 0.53$ eV) and in the third (for $M_\nu = 0.53$ eV) scenarios; PICO in the first (for $M_\nu = 0.53$ eV), the second (for $M_\nu = 0.53$ eV) and in the third (for $M_\nu = 0.53$ eV) scenarios.

These results indicate that with advancements in nonlinear modelling, substantial enhancements in the characterisation of this cross-correlation can be obtained. Such improvements would enable results comparable to those achieved with GC and CMBL for the detection of the ISWRS and the identification of M_ν .

3.5 CMB-Lensing

The investigation of the cross-correlation between CMBL and the ISWRS effect has on the one hand the advantages of a larger sky fraction and of an extremely larger superposition between the window functions (Figure 1), while on the other hand the CMBL comes with the cost of a non-negligible reconstruction noise, that significantly affects this detection. However, the next generation CMB experiments aim to achieve unprecedented noise levels, as illustrated in Figure 5, which are expected to greatly enhance detection capabilities.

3.5.1 CMBL \times ISWRS

Figure 12 shows the most outstanding results from this study. This is due to the fact that the CMBL reconstruction noise of CMB-HD is significantly lower than that of SO, CMB-S4 and PICO, with a marked reduction at the scales relevant for the ISWRS effect. As a result, its measurement of CMBL makes it the most effective Φ -probe among those tested in this work. In this figure, we do not show results for SO, as the corresponding CMBL reconstruction noise level results in low S/N values for the cross-correlation. On the other

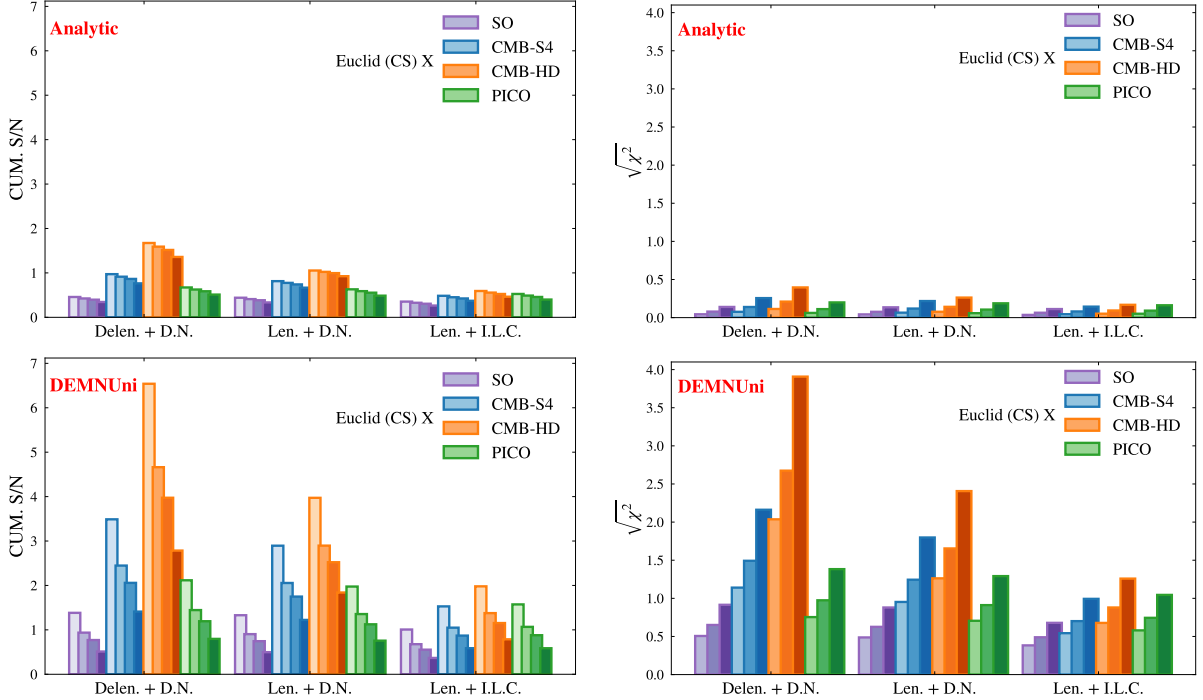


Figure 11: *Upper panels:* Same as Figure 10, but realised for the case of a massless neutrino Planck 2014b cosmology [80], generalised to four $\nu\Lambda$ CDM cases with $M_\nu = 0.0, 0.17, 0.30, 0.53$ eV. *Lower panels:* Same as the upper panels, but obtained using the cross-spectra extracted from the DEMNUni maps realised for the same cosmologies.

hand, the results achieved when mocking CMB-HD significantly overcome a 5σ detection level in all the cosmologies tested in the cases of lensed and unlensed C_ℓ^{TT} , with and without I.L.C. This makes CMB-HD a perfect machinery for the detection of the ISWRS. The results shown in the left panel reach $\sim 19\sigma$, achieved for $M_\nu = 0.06$ eV. The promising results for the detection guarantee very promising results also for the identification of the $\nu\Lambda$ CDM model, at least for $M_\nu > 0.18$ eV.

These findings concretely pave the way for using this probe to infer new constraints on neutrino masses. In our forecasts, we neglect any residual foreground contamination in the CMBL reconstruction that might correlate with foreground residuals in the CMB anisotropy map, potentially inducing a systematic bias. However, next-generation CMB experiments will obtain lensing reconstruction primarily from polarization measurements, which are significantly less prone to foreground contamination [96, 97].

4 Conclusions and discussion

In this work, we explore the possibility of detecting the ISWRS effect and use this detection to discriminate between $\nu\Lambda$ CDM models with current and next generation CMB experiments and LSS surveys.

We start by testing an ideal case. We assume to have a Φ -tracer probe whose window function $W(k, z)$ perfectly overlaps with the one of the ISWRS effect (i.e., the investigated signal is actually the ISWRS auto-spectrum, $C_\ell^{\Phi\Phi}$), a full-sky coverage and negligible sta-

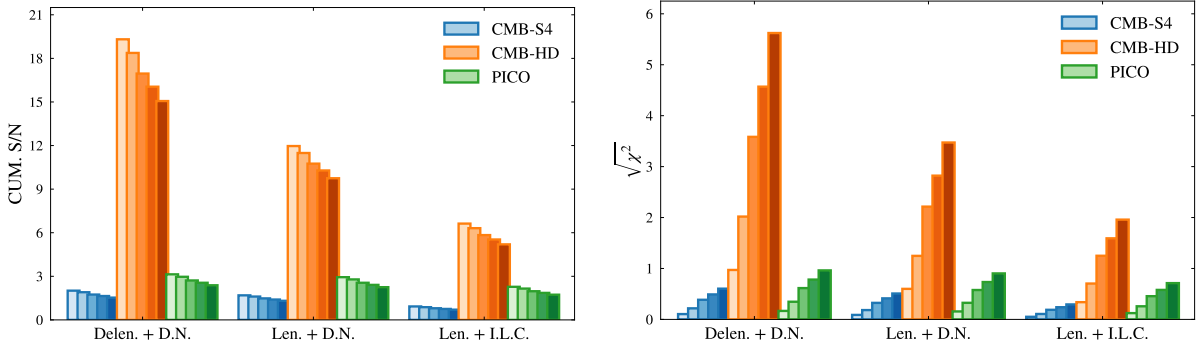


Figure 12: Same as Figure 7, but for the case of the cross-correlation between CMBL and the ISWRS effect, with both fields measured with CMB-S4, CMB-HD and PICO, for the three scenarios tested in this case. Results for SO are not shown because of the low forecasted S/N.

stistical and instrumental noises. We test these conditions using $C_\ell^{\Phi\Phi}$ extracted from the DEMNUni N-body simulations realised for the baseline Planck 2014b cosmology [80], generalised to $\nu\Lambda$ CDM models with $M_\nu = 0.0, 0.17, 0.30$ eV. The necessity to work with N-body simulations arises from the impossibility to properly represent nonlinear scales analitically. In this ideal case, not only the ISWRS effect can be detected at $\sim 100\sigma$ ($\sim 200\sigma$ if delensing techniques are applied to the CMB anisotropy field), but it is even possible to discriminate a model with $M_\nu = 0.17$ eV from the case of null mass with a $\sim 15\sigma$ significance level ($\sim 22\sigma$ if delensing techniques are applied), as shown in Figure 4.

Realistic scenarios are less ambitious, yet very promising. Our real-case analysis consists of producing forecasts of the ISWRS cross-correlation with GC, CS and CMBL that will be measured from the combination of SO, CMB-S4, CMB-HD and PICO with Euclid and LSST. To simulate these cross-power spectra, we use our analytical modelling developed in [31]. We compute them assuming a Planck 2018 baseline cosmology [4], to which we add neutrinos with total mass $M_\nu = 0.06, 0.12, 0.18, 0.24, 0.30$ eV, and using the nonlinear $P_{\delta\delta}(k, z)$ computed with the Takahashi model [64], since we have verified that it works better for the reconstruction of the cross-correlations analysed in our previous work [31]. We test three different scenarios, that account for an increasingly realistic and complete description of the sources of confusion for the measurement, starting from considering only the impact of primary CMB anisotropies, then adding detector noise, and finally also possible residual foregrounds. For the case of the cross-correlation with GC only, we test a fourth scenario, where we apply an optimal weighting to reshape the galaxy distribution to increase the overlap between the ISWRS and the GC window function and minimise the noise.

We achieve the best results when analysing the cross-correlation of the ISWRS with CMBL, as measured by CMB-HD, across all tested $\nu\Lambda$ CDM cosmologies. This holds true for both lensed and delensed C_ℓ^{TT} , and whether considering only detector noise or both detector noise and foregrounds, as evident from Figure 12. The reason is that CMB-HD, despite lacking the sky coverage of a space telescope like PICO, exhibits a particularly low CMBL reconstruction noise at the scales of interest due to the high-sensitivity at high-resolution (see Figure 5). Considering the extended overlap of the CMBL and ISWRS window functions, the CMBL measured by CMB-HD proves to be a superior probe compared to all the others tested in this work. This is the first time, to our knowledge, that the detectability of the effect has been assessed in cross-correlation with CMBL. Accordingly to its promising detection results, this

cross-correlation can also allow the identification of a $\nu\Lambda$ CDM model with $M_\nu \geq 0.12$ eV, in the case of a measurement with negligible levels of residual foregrounds (current estimates point to $M_\nu < 0.11$ eV at 95% C.L.; [5]).

Another implication of the better resolution in the frequency range where CMB dominates (i.e. 70 – 150 GHz) of CMB-HD, with respect to SO, CMB-S4 and PICO, consists of having lower detector noise and foreground residuals at the scales of interest. These features make CMB-HD the best CMB experiment among those tested in this work even in combination with LSS surveys for the analysis of the other two cross-correlations (Figures 7-11). In the case of the cross-correlation with GC, we expect to reach high-significance detections for CMB-S4 and CMB-HD, provided that residual foregrounds can be kept under control. We want to highlight the significant improvement achieved when using the optimal weighting, which leads to an increase of the order of $\sim 60\%$ (on average) in the S/N ratio. We obtain the best results for this cross-correlation when combining the LSST “Optimistic” sample with CMB-HD, not only for the already mentioned advantages of this CMB experiment, but even for the high galaxy density of this LSS survey (which reduces the galaxy shot-noise), the large overlap between the observed sky fractions of the two instruments (which increases the combined f_{sky}), and the significant overlap between the ISWRS and LSST “Optimistic” sample window functions. Among the GC samples tested, LSST “Optimistic” is the only one that allows to set constraints on $\nu\Lambda$ CDM models with $M_\nu \gtrsim 0.30$ eV, even when accounting for the realistic conditions of lensed C_ℓ^{TT} , with detector noise and residual foregrounds. Moreover, it is the GC sample that reaches the best results when applying the optimal weighting, suggesting the potential of this tool, and in particular of its application to LSST.

The less promising results of this work have been achieved in the analysis of the cross-correlation between the ISWRS effect and the photometric Euclid CS survey. This is not only because the superposition between the window functions of CS and ISWRS effect is significantly lower than the case of GC (see Figure 1) while the noise is of the same order of magnitude, but also because the analytical reconstruction of this cross-correlation is less accurate with respect to the others, and in particular underestimates the results of N-body simulations. These conditions negatively affect our analysis, leading the cumulative S/N ratio to barely reach the 1σ level (Figure 10).

However, we restore confidence in the potential of the cross-correlation between the Euclid CS sample and the ISWRS effect by performing the same analysis with cross-spectra extracted from the DEMNUni N-body simulations (Figure 11). This test leads to an improved cumulative S/N ratio, enhancing the prospects for detections and restoring the feasibility of disentangling the $\nu\Lambda$ CDM models. We believe then that an improvement in the modelling of nonlinear scales is essential to improve the accuracy of our analytical reconstruction and, in particular, to produce more robust predictions of the ISWRS cross-correlation with CS.

Given that the third scenario (lensed C_ℓ^{TT} + ILC) we investigate is quite conservative and that, as of today, delensing techniques and foreground cleaning methods are becoming increasingly refined, our predictions are merely a starting point for the promising results that we can expect in the near future. Moreover, considering that even under these conditions we consistently achieve a detection in the case of cross-correlations with GC and CMBL, we feel confident that once experiments similar to those tested here will see the light, we will be able to properly detect the ISWRS. Furthermore, we verify that even CS is a valid probe for this kind of analysis, despite the technical limitations of our current study.

Overall, our method is a useful and computationally non-expensive tool to investigate the ISWRS cross-correlations with Φ -tracers in different cosmological scenarios, without the need

to run large N-body simulations for each cosmology.

Acknowledgments

VC and MM acknowledge support by the INFN project “InDark”. MM is also supported by the ASI/LiteBIRD grant n.2020-9-HH.0. The DEMNUni simulations were carried out in the framework of “The Dark Energy and Massive-Neutrino Universe” project, using the Tier-0 IBM BG/Q Fermi machine and the Tier-0 Intel OmniPath Cluster Marconi-A1 of the Centro Interuniversitario del Nord-Est per il Calcolo Elettronico (CINECA). We acknowledge a generous CPU and storage allocation by the Italian Super-Computing Resource Allocation (ISCRA) as well as from the coordination of the “Accordo Quadro MoU per lo svolgimento di attività congiunta di ricerca Nuove frontiere in Astrofisica: HPC e Data Exploration di nuova generazione”, together with storage from INFN-CNAF and INAF-IA2.

A Validation of the ISWRS cross-correlation with CS

Following the procedure implemented in [31], we validate Equation (2.7b) against DEMNUni simulations. We use a set of correlated DEMNUni maps, composed of an ISWRS map and a CS map, realised with the techniques described in [93–95], characterised by the baseline Planck 2014b [80] cosmology, with $M_\nu = 0.0$ eV, in the redshift range that goes from $z_{min} = 0.2$ to $z_{max} = 2.5$. We analytically compute the expected cross-angular power spectrum between ISWRS and CS using CAMB for all the ingredients of Equation (2.7b) (assuming the same cosmology as in DEMNUni maps), apart from $n(z)$ given by Equation (2.10a), which is the galaxy selection used to realise the CS DEMNUni map. For this computation, we test both the Takahashi [64] and the Mead2020 [77] Halofit [63] modellings. Compared with the cross-power spectrum extracted from the DEMNUni maps, the overall shape of the spectrum and the amplitude at very large scales are accurately recovered (see Figure 13). However, differently from the results presented in [31], where the cross-correlations of ISWRS with GC and CMBL were validated, the discrepancies in the position of the sign inversion and the amplitude at small scales are more pronounced. This is likely because the CS field is more sensitive to nonlinearities, and the assumptions made in the considered Halofit models do not offer precise reconstructions of nonlinear scales for this cross-correlation. This mismatch at small scales is responsible for our discouraging results of Section 3.4.

B Cross angular power spectra

The cross angular power spectrum between two fields **A** and **B** can be written as [53, 98]:

$$C_\ell^{AB} = \frac{2}{\pi} \int dk \int dz \int dz' k^2 P_{\delta\delta}(k, z, z') W^A(k, z) j_\ell[k \chi(z)] W^B(k, z') j_\ell[k \chi(z')], \quad (\text{B.1})$$

where $j_\ell[k \chi(z)]$ are the Bessel functions and $W(k, z)$ are the window functions of the selected fields. The Limber approximation allows us to have [53, 57]:

$$\int dk k^2 P_{\delta\delta}(k, z, z') j_\ell[k \chi(z)] j_\ell[k \chi(z')] \simeq \frac{\pi}{2} k^2 \delta_D(z - z') \frac{H(z)}{c} \frac{1}{k^2 \chi^2(z)} P_{\delta\delta} \left(k = \frac{\ell + 1/2}{\chi(z)}, z \right)$$

where we have used:

$$\delta_D[\chi(z) - \chi(z')] = \delta_D(z - z') \frac{H(z)}{c},$$

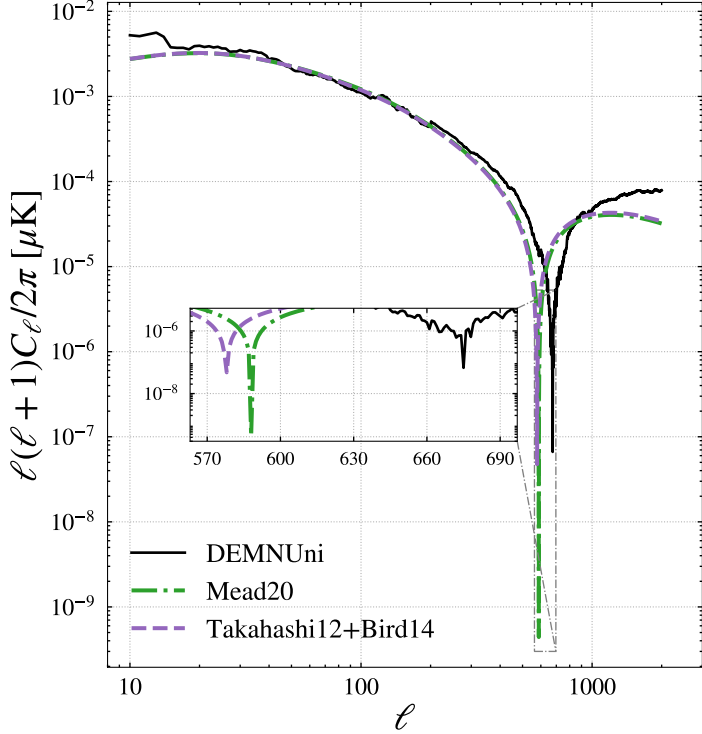


Figure 13: Angular power spectrum obtained from the DEMNUni maps (solid black line), compared with the analytical predictions computed with both the Takahashi12+Bird14 [64] (dashed violet) and the Mead20 [77] (dot-dashed green) Halofit models.

in the Dirac delta, given that:

$$\chi(z) = \int dz' \frac{c}{H(z')}.$$

Fixing now:

$$k = \frac{\ell + 1/2}{\chi(z)}, \quad (\text{B.2})$$

equation (B.1) becomes then:

$$C_\ell^{AB} = \int dz \frac{H(z)}{c \chi^2(z)} W^A(k, z) W^B(k, z) P_{\delta\delta}(k, z). \quad (\text{B.3})$$

However, in the case of the cross-correlation between the ISWRS effect ($\dot{\Phi}$) and a gravitational potential tracer \mathbf{Y} , we have to compute:

$$C_\ell^{\dot{\Phi}Y} = -2 \int dz \frac{H(z)}{c \chi^2(z)} W_Y(z) P_{\dot{\Phi},\delta}(k, z), \quad (\text{B.4})$$

where the factor (-2) comes from Equation (2.1) (neglecting $e^{-\tau(z)}$ [49]).

Starting from the Poisson's equation [28] expressed as a function of t :

$$\Phi(k, t) = -\frac{3}{2} \Omega_m \left(\frac{H_0}{c k} \right)^2 \frac{\delta(k, t)}{a(t)},$$

one can derive:

$$\delta(k, t) = -\frac{a(t)}{F(k)} \Phi(k, t),$$

with

$$F(k) = \frac{3}{2} \Omega_m \left(\frac{H_0}{c k} \right)^2. \quad (\text{B.5})$$

We have then [53]:

$$\begin{aligned} P_{\delta, \dot{\Phi}}(k, t) &= \left\langle \delta(k, t), \dot{\Phi}(k, t) \right\rangle = \\ &= -\frac{a(t)}{F(k)} \langle \Phi(k, t), \dot{\Phi}(k, t) \rangle = \\ &= -\frac{a(t)}{F(k)} P_{\Phi, \dot{\Phi}}(k, t) = \\ &\simeq -\frac{a(t)}{F(k)} \frac{1}{2} \partial_t [P_{\Phi, \Phi}(k, t)] = \\ &\simeq -a(t) F(k) \frac{1}{2} \partial_t \left[\frac{P_{\delta, \delta}(k, t)}{a^2(t)} \right] \end{aligned}$$

where we use $P_{\Phi, \Phi}(k, t) = \left(\frac{F(k)}{a(t)} \right)^2 P_{\delta, \delta}(k, t)$ and $P_{\Phi, \dot{\Phi}}(k, t) \simeq \frac{1}{2} \partial_t [P_{\Phi, \Phi}(k, t)]$ [53, 78]. Making now a coordinates transformation from t to z , we have:

$$(-2) W_Y(z) P_{\delta, \dot{\Phi}}(k, z) = \frac{3}{2} \Omega_m \left(\frac{H_0}{c k} \right)^2 a(z) W_Y(z) \left[\partial_z \frac{P_{\delta, \delta}(k, z)}{a^2(z)} \right],$$

that with the proper $W_Y(z)$ from Equations (2.3) results in Equations (2.7).

References

- [1] E.V. Linder, *Exploring the Expansion History of the Universe*, *Phys. Rev. Lett.* **90** (2003) 091301 [[astro-ph/0208512](#)].
- [2] J. Lesgourgues and S. Pastor, *Neutrino mass from Cosmology*, *arXiv e-prints* (2012) arXiv:1212.6154 [[1212.6154](#)].
- [3] M. Archidiacono, S. Hannestad and J. Lesgourgues, *What will it take to measure individual neutrino mass states using cosmology?*, *J. Cosmology Astropart. Phys.* **2020** (2020) 021 [[2003.03354](#)].
- [4] Planck Collaboration, N. Aghanim, Y. Akrami, M. Ashdown, J. Aumont, C. Baccigalupi et al., *Planck 2018 results. VI. Cosmological parameters*, *A&A* **641** (2020) A6 [[1807.06209](#)].
- [5] I.J. Allali and A. Notari, *Neutrino mass bounds from DESI 2024 are relaxed by Planck PR4 and cosmological supernovae*, *arXiv e-prints* (2024) arXiv:2406.14554 [[2406.14554](#)].
- [6] W. Elbers, A. Aviles, H.E. Noriega, D. Chebat, A. Menegas, C.S. Frenk et al., *Constraints on Neutrino Physics from DESI DR2 BAO and DR1 Full Shape*, *arXiv e-prints* (2025) arXiv:2503.14744 [[2503.14744](#)].
- [7] R.K. Sachs and A.M. Wolfe, *Perturbations of a Cosmological Model and Angular Variations of the Microwave Background*, *ApJ* **147** (1967) 73.
- [8] M.J. Rees and D.W. Sciama, *Large-scale Density Inhomogeneities in the Universe*, *Nature* **217** (1968) 511.

[9] A.A. Penzias and R.W. Wilson, *A Measurement of Excess Antenna Temperature at 4080 Mc/s.*, [ApJ 142 \(1965\) 419](#).

[10] S. Ferraro, B.D. Sherwin and D.N. Spergel, *WISE measurement of the integrated Sachs-Wolfe effect*, [Phys. Rev. D 91 \(2015\) 083533 \[1401.1193\]](#).

[11] T. Giannantonio, R. Scranton, R.G. Crittenden, R.C. Nichol, S.P. Boughn, A.D. Myers et al., *Combined analysis of the integrated Sachs-Wolfe effect and cosmological implications*, [Phys. Rev. D 77 \(2008\) 123520 \[0801.4380\]](#).

[12] T. Giannantonio, R. Crittenden, R. Nichol and A.J. Ross, *The significance of the integrated Sachs-Wolfe effect revisited*, [MNRAS 426 \(2012\) 2581 \[1209.2125\]](#).

[13] W.A. Watson, J.M. Diego, S. Gottlöber, I.T. Iliev, A. Knebe, E. Martínez-González et al., *The Jubilee ISW project - I. Simulated ISW and weak lensing maps and initial power spectra results*, [MNRAS 438 \(2014\) 412 \[1307.1712\]](#).

[14] K. Naidoo, P. Fosalba, L. Whiteway and O. Lahav, *Full-sky integrated Sachs-Wolfe maps for the MICE grand challenge lightcone simulation*, [MNRAS 506 \(2021\) 4344 \[2103.14654\]](#).

[15] R. Kimura, T. Kobayashi and K. Yamamoto, *Observational constraints on kinetic gravity braiding from the integrated Sachs-Wolfe effect*, [Phys. Rev. D 85 \(2012\) 123503 \[1110.3598\]](#).

[16] S. Nakamura, A. De Felice, R. Kase and S. Tsujikawa, *Constraints on massive vector dark energy models from integrated Sachs-Wolfe-galaxy cross-correlations*, [Phys. Rev. D 99 \(2019\) 063533 \[1811.07541\]](#).

[17] J.A. Kable, G. Benevento, N. Frusciante, A. De Felice and S. Tsujikawa, *Probing modified gravity with integrated Sachs-Wolfe CMB and galaxy cross-correlations*, [J. Cosmology Astropart. Phys. 2022 \(2022\) 002 \[2111.10432\]](#).

[18] T.L. Smith, J.T. Giblin, M. Amin, M. Gerhardinger, E. Florio, M. Cerep et al., *Novel integrated Sachs-Wolfe effect from early dark energy*, [Phys. Rev. D 108 \(2023\) 123534 \[2304.02028\]](#).

[19] M. Kamionkowski, *Matter-microwave correlations in an open universe*, [Phys. Rev. D 54 \(1996\) 4169 \[astro-ph/9602150\]](#).

[20] J.R. Bond, G. Efstathiou and J. Silk, *Massive neutrinos and the large-scale structure of the universe*, [Phys. Rev. Lett. 45 \(1980\) 1980](#).

[21] R.G. Crittenden and N. Turok, *Looking for a Cosmological Constant with the Rees-Sciama Effect*, [Phys. Rev. Lett. 76 \(1996\) 575 \[astro-ph/9510072\]](#).

[22] R. Kneissl, R. Egger, G. Hasinger, A.M. Soltan and J. Truemper, *Search for correlations between COBE DMR and ROSAT PSPC all-sky survey data.*, [A&A 320 \(1997\) 685 \[astro-ph/9610160\]](#).

[23] S.P. Boughn, R.G. Crittenden and N.G. Turok, *Correlations between the cosmic X-ray and microwave backgrounds: constraints on a cosmological constant*, [New A 3 \(1998\) 275 \[astro-ph/9704043\]](#).

[24] S.P. Boughn and R.G. Crittenden, *Cross Correlation of the Cosmic Microwave Background with Radio Sources: Constraints on an Accelerating Universe*, [Phys. Rev. Lett. 88 \(2001\) 021302 \[astro-ph/0111281\]](#).

[25] S. Boughn and R. Crittenden, *A correlation between the cosmic microwave background and large-scale structure in the Universe*, [Nature 427 \(2004\) 45 \[astro-ph/0305001\]](#).

[26] J. Lesgourgues, W. Valkenburg and E. Gaztañaga, *Constraining neutrino masses with the integrated-Sachs-Wolfe-galaxy correlation function*, [Phys. Rev. D 77 \(2008\) 063505 \[0710.5525\]](#).

[27] M. Douspis, P.G. Castro, C. Caprini and N. Aghanim, *Optimising large galaxy surveys for ISW detection*, [A&A 485 \(2008\) 395 \[0802.0983\]](#).

[28] Y.-C. Cai, S. Cole, A. Jenkins and C.S. Frenk, *Full-sky map of the ISW and Rees-Sciama effect from Gpc simulations*, [MNRAS **407** \(2010\) 201](#) [[1003.0974](#)].

[29] A.J. Nishizawa, *The integrated Sachs-Wolfe effect and the Rees-Sciama effect*, [Progress of Theoretical and Experimental Physics **2014** \(2014\) 06B110](#) [[1404.5102](#)].

[30] C. Carbone, M. Petkova and K. Dolag, *DEMNUni: ISW, Rees-Sciama, and weak-lensing in the presence of massive neutrinos*, [J. Cosmology Astropart. Phys. **2016** \(2016\) 034](#) [[1605.02024](#)].

[31] V. Cuozzo, C. Carbone, M. Calabrese, E. Carella and M. Migliaccio, *DEMNUni: cross-correlating the nonlinear ISWRS effect with CMB-lensing and galaxies in the presence of massive neutrinos*, [J. Cosmology Astropart. Phys. **2024** \(2024\) 073](#) [[2307.15711](#)].

[32] S.C. Hotinli, J. Meyers, C. Trendafilova, D. Green and A. van Engelen, *The benefits of CMB delensing*, [J. Cosmology Astropart. Phys. **2022** \(2022\) 020](#) [[2111.15036](#)].

[33] G. Puglisi, G. Mihaylov, G.V. Panopoulou, D. Poletti, J. Errard, P.A. Puglisi et al., *Improved galactic foreground removal for B-mode detection with clustering methods*, [MNRAS **511** \(2022\) 2052](#) [[2109.11562](#)].

[34] T. Louis, A. La Posta, Z. Atkins, H.T. Jense, I. Abril-Cabezas, G.E. Addison et al., *The Atacama Cosmology Telescope: DR6 Power Spectra, Likelihoods and Λ CDM Parameters*, [arXiv e-prints](#) (2025) arXiv:2503.14452 [[2503.14452](#)].

[35] S.K. Choi, M. Hasselfield, S.-P.P. Ho, B. Koopman, M. Lungu, M.H. Abitbol et al., *The Atacama Cosmology Telescope: a measurement of the Cosmic Microwave Background power spectra at 98 and 150 GHz*, [J. Cosmology Astropart. Phys. **2020** \(2020\) 045](#) [[2007.07289](#)].

[36] E. Camphuis, W. Quan, L. Balkenhol, A.R. Khalife, F. Ge, F. Guidi et al., *SPT-3G D1: CMB temperature and polarization power spectra and cosmology from 2019 and 2020 observations of the SPT-3G Main field*, [arXiv e-prints](#) (2025) arXiv:2506.20707 [[2506.20707](#)].

[37] S. Ferraro, E. Schaan and E. Pierpaoli, *Is the Rees-Sciama effect detectable by the next generation of cosmological experiments?*, [arXiv e-prints](#) (2022) arXiv:2205.10332 [[2205.10332](#)].

[38] P. Ade, J. Aguirre, Z. Ahmed, S. Aiola, A. Ali, D. Alonso et al., *The Simons Observatory: science goals and forecasts*, [J. Cosmology Astropart. Phys. **2019** \(2019\) 056](#) [[1808.07445](#)].

[39] A. Lee, M.H. Abitbol and S. Adachi et al., *The Simons Observatory*, in *Bulletin of the American Astronomical Society*, vol. 51, p. 147, Sept., 2019 [[1907.08284](#)].

[40] K. Abazajian, G. Addison, P. Adshead, Z. Ahmed, S.W. Allen, D. Alonso et al., *CMB-S4 Science Case, Reference Design, and Project Plan*, [arXiv e-prints](#) (2019) arXiv:1907.04473 [[1907.04473](#)].

[41] K.N. Abazajian, P. Adshead, Z. Ahmed, S.W. Allen, D. Alonso, K.S. Arnold et al., *CMB-S4 Science Book, First Edition*, [arXiv e-prints](#) (2016) arXiv:1610.02743 [[1610.02743](#)].

[42] N. Sehgal, S. Aiola, Y. Akrami, K. Basu, M. Boylan-Kolchin, S. Bryan et al., *CMB-HD: An Ultra-Deep, High-Resolution Millimeter-Wave Survey Over Half the Sky*, in *Bulletin of the American Astronomical Society*, vol. 51, p. 6, Sept., 2019, DOI [[1906.10134](#)].

[43] The CMB-HD Collaboration, :, S. Aiola, Y. Akrami, K. Basu, M. Boylan-Kolchin et al., *Snowmass2021 CMB-HD White Paper*, [arXiv e-prints](#) (2022) arXiv:2203.05728 [[2203.05728](#)].

[44] S. Hanany, M. Alvarez, E. Artis, P. Ashton, J. Aumont, R. Aulien et al., *PICO: Probe of Inflation and Cosmic Origins*, [arXiv e-prints](#) (2019) arXiv:1902.10541 [[1902.10541](#)].

[45] R. Aulien, M. Remazeilles, S. Belkner, J. Carron, J. Delabrouille, H.K. Eriksen et al., *Foreground separation and constraints on primordial gravitational waves with the PICO space mission*, [J. Cosmology Astropart. Phys. **2023** \(2023\) 034](#) [[2211.14342](#)].

[46] Euclid Collaboration, Y. Mellier, Abdurro'uf, J.A. Acevedo Barroso, A. Achúcarro, J. Adamek et al., *Euclid. I. Overview of the Euclid mission*, *arXiv e-prints* (2024) arXiv:2405.13491 [2405.13491].

[47] LSST Science Collaboration, P.A. Abell, J. Allison, S.F. Anderson, J.R. Andrew, J.R.P. Angel et al., *LSST Science Book, Version 2.0*, *arXiv e-prints* (2009) arXiv:0912.0201 [0912.0201].

[48] The LSST Dark Energy Science Collaboration, R. Mandelbaum, T. Eifler, R. Hložek, T. Collett, E. Gawiser et al., *The LSST Dark Energy Science Collaboration (DESC) Science Requirements Document*, *arXiv e-prints* (2018) arXiv:1809.01669 [1809.01669].

[49] B. Stölzner, A. Cuoco, J. Lesgourges and M. Bilicki, *Updated tomographic analysis of the integrated Sachs-Wolfe effect and implications for dark energy*, *Phys. Rev. D* **97** (2018) 063506 [1710.03238].

[50] G. Rossi, N. Palanque-Delabrouille, A. Borde, M. Viel, C. Yèche, J.S. Bolton et al., *Suite of hydrodynamical simulations for the Lyman- α forest with massive neutrinos*, *A&A* **567** (2014) A79 [1401.6464].

[51] Euclid Collaboration, A. Blanchard, S. Camera, C. Carbone, V.F. Cardone, S. Casas et al., *Euclid preparation. VII. Forecast validation for Euclid cosmological probes*, *A&A* **642** (2020) A191 [1910.09273].

[52] G. Piccirilli, M. Migliaccio, E. Branchini and A. Dolfi, *A cross-correlation analysis of CMB lensing and radio galaxy maps*, *A&A* **671** (2023) A42 [2208.07774].

[53] R.E. Smith, C. Hernández-Monteagudo and U. Seljak, *Impact of scale dependent bias and nonlinear structure growth on the integrated Sachs-Wolfe effect: Angular power spectra*, *Phys. Rev. D* **80** (2009) 063528 [0905.2408].

[54] Planck Collaboration, P.A.R. Ade, N. Aghanim, M. Arnaud, M. Ashdown, J. Aumont et al., *Planck 2015 results. XIII. Cosmological parameters*, *A&A* **594** (2016) A13 [1502.01589].

[55] Planck Collaboration, N. Aghanim, Y. Akrami, M. Ashdown, J. Aumont, C. Baccigalupi et al., *Planck 2018 results. VIII. Gravitational lensing*, *A&A* **641** (2020) A8 [1807.06210].

[56] A. Mangilli and L. Verde, *Non-Gaussianity and the CMB bispectrum: Confusion between primordial and lensing-Rees-Sciama contribution?*, *Phys. Rev. D* **80** (2009) 123007 [0906.2317].

[57] D.N. Limber, *The Analysis of Counts of the Extragalactic Nebulae in Terms of a Fluctuating Density Field.*, *ApJ* **117** (1953) 134.

[58] I. Tutusaus, M. Martinelli, V.F. Cardone, S. Camera, S. Yahia-Cherif, S. Casas et al., *Euclid: The importance of galaxy clustering and weak lensing cross-correlations within the photometric Euclid survey*, *A&A* **643** (2020) A70 [2005.00055].

[59] A. Gorecki, A. Abate, R. Ansari, A. Barrau, S. Baumont, M. Moniez et al., *A new method to improve photometric redshift reconstruction. Applications to the Large Synoptic Survey Telescope*, *A&A* **561** (2014) A128 [1301.3010].

[60] B. Yu, R.Z. Knight, B.D. Sherwin, S. Ferraro, L. Knox and M. Schmittfull, *Towards Neutrino Mass from Cosmology without Optical Depth Information*, *arXiv e-prints* (2018) arXiv:1809.02120 [1809.02120].

[61] B. Yu, S. Ferraro, Z.R. Knight, L. Knox and B.D. Sherwin, *The physical origin of dark energy constraints from Rubin Observatory and CMB-S4 lensing tomography*, *MNRAS* **513** (2022) 1887 [2108.02801].

[62] A. Lewis and A. Challinor, “CAMB: Code for Anisotropies in the Microwave Background.” *Astrophysics Source Code Library*, record ascl:1102.026, Feb., 2011.

[63] R.E. Smith, J.A. Peacock, A. Jenkins, S.D.M. White, C.S. Frenk, F.R. Pearce et al., *Stable*

clustering, the halo model and non-linear cosmological power spectra, [MNRAS **341** \(2003\) 1311](#) [[astro-ph/0207664](#)].

- [64] R. Takahashi, M. Sato, T. Nishimichi, A. Taruya and M. Oguri, *Revising the Halofit Model for the Nonlinear Matter Power Spectrum*, [ApJ **761** \(2012\) 152](#) [[1208.2701](#)].
- [65] S. Bird, M. Viel and M.G. Haehnelt, *Massive neutrinos and the non-linear matter power spectrum*, [MNRAS **420** \(2012\) 2551](#) [[1109.4416](#)].
- [66] E. Castorina, C. Carbone, J. Bel, E. Sefusatti and K. Dolag, *DEMNUni: the clustering of large-scale structures in the presence of massive neutrinos*, [J. Cosmology Astropart. Phys. **2015** \(2015\) 043](#) [[1505.07148](#)].
- [67] M. Moresco, F. Marulli, L. Moscardini, E. Branchini, A. Cappi, I. Davidzon et al., *The VIMOS Public Extragalactic Redshift Survey (VIPERS) . Exploring the dependence of the three-point correlation function on stellar mass and luminosity at $0.5 < z < 1.1$* , [A&A **604** \(2017\) A133](#) [[1603.08924](#)].
- [68] M. Zennaro, J. Bel, J. Dossett, C. Carbone and L. Guzzo, *Cosmological constraints from galaxy clustering in the presence of massive neutrinos*, [MNRAS **477** \(2018\) 491](#) [[1712.02886](#)].
- [69] R. Ruggeri, E. Castorina, C. Carbone and E. Sefusatti, *DEMNUni: massive neutrinos and the bispectrum of large scale structures*, [J. Cosmology Astropart. Phys. **2018** \(2018\) 003](#) [[1712.02334](#)].
- [70] J. Bel, A. Pezzotta, C. Carbone, E. Sefusatti and L. Guzzo, *Accurate fitting functions for peculiar velocity spectra in standard and massive-neutrino cosmologies*, [A&A **622** \(2019\) A109](#) [[1809.09338](#)].
- [71] G. Parimbelli, S. Anselmi, M. Viel, C. Carbone, F. Villaescusa-Navarro, P.S. Corasaniti et al., *The effects of massive neutrinos on the linear point of the correlation function*, [J. Cosmology Astropart. Phys. **2021** \(2021\) 009](#) [[2007.10345](#)].
- [72] G. Parimbelli, C. Carbone, J. Bel, B. Bose, M. Calabrese, E. Carella et al., *DEMNUni: comparing nonlinear power spectra prescriptions in the presence of massive neutrinos and dynamical dark energy*, [J. Cosmology Astropart. Phys. **2022** \(2022\) 041](#) [[2207.13677](#)].
- [73] P. Baratta, J. Bel, S. Gouyou Beauchamps and C. Carbone, *COVMOS: A new Monte Carlo approach for galaxy clustering analysis*, [A&A **673** \(2023\) A1](#) [[2211.13590](#)].
- [74] M. Guidi, A. Veropalumbo, E. Branchini, A. Eggemeier and C. Carbone, *Modelling the next-to-leading order matter three-point correlation function using FFTLog*, [J. Cosmology Astropart. Phys. **2023** \(2023\) 066](#) [[2212.07382](#)].
- [75] S. Gouyou Beauchamps, P. Baratta, S. Escoffier, W. Gillard, J. Bel, J. Bautista et al., *Cosmological inference including massive neutrinos from the matter power spectrum: biases induced by uncertainties in the covariance matrix*, [arXiv e-prints](#) (2023) [arXiv:2306.05988](#) [[2306.05988](#)].
- [76] E. Carella, C. Carbone, M. Zennaro, G. Girelli, M. Bolzonella, F. Marulli et al., *DEMNUni: The galaxy-halo connection in the presence of dynamical dark energy and massive neutrinos*, *In prep.*
- [77] A.J. Mead, S. Brieden, T. Tröster and C. Heymans, *HMCODE-2020: improved modelling of non-linear cosmological power spectra with baryonic feedback*, [MNRAS **502** \(2021\) 1401](#) [[2009.01858](#)].
- [78] A.J. Nishizawa, E. Komatsu, N. Yoshida, R. Takahashi and N. Sugiyama, *Cosmic Microwave Background-Weak Lensing Correlation: Analytical and Numerical Study of Nonlinearity and Implications for Dark Energy*, [ApJ **676** \(2008\) L93](#) [[0711.1696](#)].

[79] B.M. Schäfer, A.F. Kalovidouris and L. Heisenberg, *Parameter estimation biases due to contributions from the Rees-Sciama effect to the integrated Sachs-Wolfe spectrum*, [MNRAS **416** \(2011\) 1302](#) [[1010.1096](#)].

[80] Planck Collaboration, P.A.R. Ade, N. Aghanim, C. Armitage-Caplan, M. Arnaud, M. Ashdown et al., *Planck 2013 results. XVI. Cosmological parameters*, [A&A **571** \(2014\) A16](#) [[1303.5076](#)].

[81] K.N. Abazajian, P. Adshead, Z. Ahmed, S.W. Allen, D. Alonso, K.S. Arnold et al., *CMB-S4 Science Book, First Edition*, [arXiv e-prints](#) (2016) arXiv:1610.02743 [[1610.02743](#)].

[82] A. MacInnis, N. Sehgal and M. Rothermel, *Cosmological parameter forecasts for a CMB-HD survey*, [Phys. Rev. D **109** \(2024\) 063527](#) [[2309.03021](#)].

[83] F. Finelli, M. Bucher, A. Achúcarro, M. Ballardini, N. Bartolo, D. Baumann et al., *Exploring cosmic origins with CORE: Inflation*, [J. Cosmology Astropart. Phys. **2018** \(2018\) 016](#) [[1612.08270](#)].

[84] C.L. Bennett, R.S. Hill, G. Hinshaw, M.R. Nolta, N. Odegard, L. Page et al., *First-Year Wilkinson Microwave Anisotropy Probe (WMAP) Observations: Foreground Emission*, [ApJS **148** \(2003\) 97](#) [[astro-ph/0302208](#)].

[85] C. Vargas, C.H. López-Caraballo, E.S. Battistelli, R. Dunner, G. Farren, M. Gralla et al., *The Atacama Cosmology Telescope: Extragalactic Point Sources in the Southern Surveys at 150, 220 and 280 GHz observed between 2008-2010*, [arXiv e-prints](#) (2023) arXiv:2310.17535 [[2310.17535](#)].

[86] L. Balkenhol, D. Dutcher, A. Spurio Mancini, A. Doussot, K. Benabed, S. Galli et al., *Measurement of the CMB temperature power spectrum and constraints on cosmology from the SPT-3G 2018 T T , T E , and E E dataset*, [Phys. Rev. D **108** \(2023\) 023510](#) [[2212.05642](#)].

[87] Euclid Collaboration, S. Ilić, N. Aghanim, C. Baccigalupi, J.R. Bermejo-Climent, G. Fabbian et al., *Euclid preparation. XV. Forecasting cosmological constraints for the Euclid and CMB joint analysis*, [A&A **657** \(2022\) A91](#) [[2106.08346](#)].

[88] B. Joachimi and S.L. Bridle, *Simultaneous measurement of cosmology and intrinsic alignments using joint cosmic shear and galaxy number density correlations*, [A&A **523** \(2010\) A1](#) [[0911.2454](#)].

[89] R. Allison, P. Caucal, E. Calabrese, J. Dunkley and T. Louis, *Towards a cosmological neutrino mass detection*, [Phys. Rev. D **92** \(2015\) 123535](#) [[1509.07471](#)].

[90] J.R. Bermejo-Climent, M. Ballardini, F. Finelli, D. Paoletti, R. Maartens, J.A. Rubiño-Martín et al., *Cosmological parameter forecasts by a joint 2D tomographic approach to CMB and galaxy clustering*, [Phys. Rev. D **103** \(2021\) 103502](#) [[2106.05267](#)].

[91] D. Alonso, G. Cusin, P.G. Ferreira and C. Pitrou, *Detecting the anisotropic astrophysical gravitational wave background in the presence of shot noise through cross-correlations*, [Phys. Rev. D **102** \(2020\) 023002](#) [[2002.02888](#)].

[92] F.R. Urban, S. Camera and D. Alonso, *Detecting ultra-high-energy cosmic ray anisotropies through harmonic cross-correlations*, [A&A **652** \(2021\) A41](#) [[2005.00244](#)].

[93] C. Carbone, V. Springel, C. Baccigalupi, M. Bartelmann and S. Matarrese, *Full-sky maps for gravitational lensing of the cosmic microwave background*, [MNRAS **388** \(2008\) 1618](#) [[0711.2655](#)].

[94] M. Calabrese, C. Carbone, G. Fabbian, M. Baldi and C. Baccigalupi, *Multiple lensing of the cosmic microwave background anisotropies*, [J. Cosmology Astropart. Phys. **2015** \(2015\) 049](#) [[1409.7680](#)].

[95] G. Fabbian, M. Calabrese and C. Carbone, *CMB weak-lensing beyond the Born approximation: a numerical approach*, [J. Cosmology Astropart. Phys. **2018** \(2018\) 050](#) [[1702.03317](#)].

- [96] N. Sailer, S. Ferraro and E. Schaan, *Foreground-immune cmb lensing reconstruction with polarization*, [*Phys. Rev. D* **107** \(2023\) 023504](#).
- [97] F.J. Qu, M. Millea and E. Schaan, *Impact and mitigation of polarized extragalactic foregrounds on bayesian cosmic microwave background lensing*, [*Phys. Rev. D* **111** \(2025\) 023503](#).
- [98] Planck Collaboration, P.A.R. Ade, N. Aghanim, M. Arnaud, M. Ashdown, J. Aumont et al., *Planck 2015 results. XXI. The integrated Sachs-Wolfe effect*, [*A&A* **594** \(2016\) A21](#) [[1502.01595](#)].